Politecnico di Torino

Politecnico di Torino

Laurea Magistrale in Ingegneria Aerospaziale

A.a. 2024/2025

Sessione di laurea 11 Dicembre 2025

Numerical Modelling of Dielectric Barrier Discharge Plasma Actuators

Relatore: Domenic D'Ambrosio

Candidato: Luca Iposi

Abstract

Dielectric Barrier Discharge plasma actuators are one of the most promising techniques of active flow control. They act by ionizing the air around them and generating a body force on the fluid which can be used to manipulate the airflow. Due to their many advantages, most of all their capability of inducing a self-limiting discharge, DBDs have multiple applications in aerodynamics, from delaying flow separation to enhancing jet mixing. Despite the interest that these actuators have drawn in the last couple of decades, the phenomena that they generate are not fully understood. Because of this, many models have been developed to study their operation. These models can be either phenomenological if they focus on the effect that the actuator has on the airflow, or first-principles based if they focus on the processes of plasma creation and evolution. In this thesis, we present a physical and chemical model for DBDs, based on the coupling between a Boltzmann Equation for electron energy distribution and a system of continuity equations for charged particles in their Drift-Diffusion approximation. A Local Field Approximation is applied to simplify the computation of transport and chemical properties, while only the most relevant chemical processes have been considered. A numerical scheme to solve such model is then described, with reflections on temporal scales and explicit and implicit methods. Finally, a collection of significant results is presented for the classical DBD configuration, known as Single-Dielectric Barrier Discharge actuator. A number of interesting parameters are computed and discussed, such as charge density, electric potential, and the body force exerted on the external flow, in order to understand the operational process of DBDs and the influence that input parameters, such as voltage and the relative dielectric constant, have on these actuators.

Table of Contents

List of Figures

Chapter 1

Introduction

Flow control has been at the center of aerodynamic research since the 1930s with the aim to improve aircraft performance and efficiency, and, recently, with the interest in reducing carbon emissions. Flow control techniques can be categorized into passive, which do not require an external power source, and active, which do.

Among these techniques, one of the most promising is plasma actuators, whose working principle consists in ionizing the surrounding air to modify its properties and control its behaviour. These are zero-net-mass-flux actuators, meaning that they can transfer momentum to the outside flow without the need for mass injection. They are generally low-cost, lightweight, low power-consuming, and do not require moving mechanical or pneumatical parts, thus drastically simplifying their structure and operation with respect to other actuators.

Other devices for active flow control are the Lorentz force actuator and the synthetic jet actuator. The latter generates high-frequency periodic wall jets by the means of rotating valves or orifices. Their main disadvantages are the use of moving parts and their need of an external flow source. The Lorentz force actuator induces a Lorentz force, through the use of sub-surface magnets, activating fluid motion. They have been proven to be very effective, however, they only work for conducting fluid and the generated force is three-dimensional and its direction can be complex to determine [1].

There are several possible types of plasma actuators, as can be seen in Ref. [2], that differ in geometry, functioning principle, and application. The three main ones are Surface Corona Discharge Actuators, Plasma Spark Jet Actuators (PSJAs), and Dielectric Barrier Discharge Actuators. The latter will be the subject of this study and are described in depth in the following pages. Surface Corona Discharge Actuators create plasma by generating an electric field around the tip of an electrode, producing a corona-type discharge. PSJAs generate sparks between two electrodes, creating a high-pressure, high-temperature zone that induces a motion in the fluid similar to a jet.

1.1 Plasma

A plasma is defined as a quasi-neutral gas of charged particles showing collective behaviour [3]. The concept of quasi-neutrality means that even though the particles making up the plasma possess charge (since they are ions and electrons), the overall charge densities even each other out to equilibrium. This is a state that the plasma actively tries to reach by moving around the charged particles in its bulk when subjected to a perturbation. Collective behaviour means that local disturbances in the equilibrium of the plasma have strong influences on distant regions of the plasma.

The plasma generated by these actuators is a so-called "highly-collisional plasma", meaning that the mean free paths of charged particles are much smaller than the discharge dimension [4] and, therefore, the electron-neutral collision frequency is greater than the plasma frequency [5]. This differs from an ideal plasma, which is collisionless i.e. plasma frequency[1] is much larger than collision frequency.

1.2 Dielectric Barrier Discharge Actuators

The most commonly used configuration is the Dielectric Barrier Discharge (DBD) due to its fast response time, non-intrusiveness, flexibility with respect to geometrical configuration, and capability to be mounted on a surface, either linear or curved, without the need to add cavities or holes. Furthermore, they can operate over a broad range of frequencies and, most importantly, they are stable at atmospheric pressure. DBDs have been studied since the second half of the 19th century originally as ozone generators [6]. It was later discovered, however, that they have multiple applications in aerodynamics such as attenuating cavity noise [7, 8], enhancing jet mixing [7], synchronizing vortex shedding behind cylinders and improving flow performance in turbines [7, 9]. They can even be paired with magnetic fluid for air purification, used as electrostatic precipitators for air filtration and employed as controlling odor gasses emission devices [10, 11, 12]. With regards to aeronautics, they have been proven to reduce drag and increase lift, therefore improving overall efficiency [13, 14, 15], control transition of boundary layers [16], and delay separation over airfoils, reattaching the external flow and moving wing stall to higher angles of attack, up to an extra 8° as demonstrated by Shengcheng et al. in [17]. They are typically used for low-speed applications, as experiments have shown good efficiency for airflow control at velocities up to 30 m/s with other

[1] Plasma electron frequency is a measure of how fast plasma responds to external disturbances and can be defined as $\omega_p = \left(\frac{q_e^2 n_e}{\epsilon_0 m_e}\right)^{1/2}$

significant results up to around 100 m/s [18]. Their use at higher velocities would require much more electrical power, resulting in higher costs and making them more prone to instability.

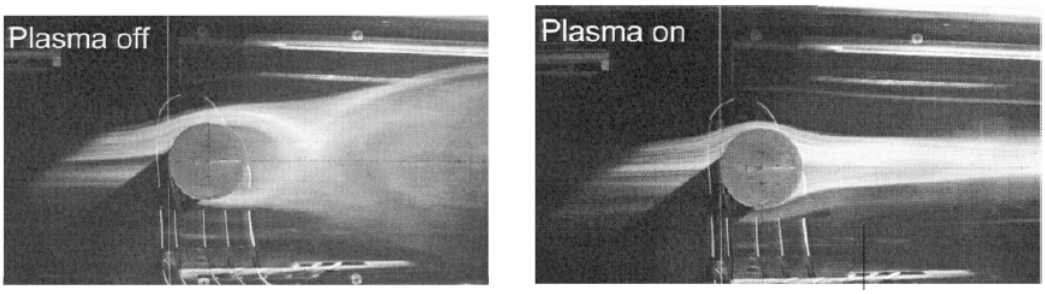

Figure 1.1: Example of DBD actuation on a cylinder wake

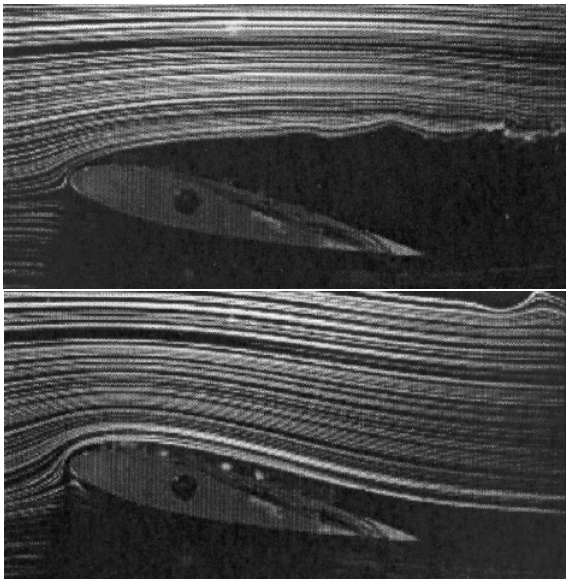

Figure 1.2: Streamlines on a NACA 0015 airfoil without (above) and with (below) DBD actuation

Single-DBDs: Geometry and Operation

Single-Dielectric Barrier Discharge plasma actuators (S-DBDs), the most widely used configuration of DBDs, are composed of two asymmetrically placed electrodes separated by a layer of dielectric material. One electrode is exposed to the outside flow, while the other is grounded and fully embedded in the dielectric. Typically, electrodes are long and thin, a few millimeters wide and arranged spanwise, while the dielectric is between 0.1 mm and a few millimeters thick [19]. It is possible to use thicker dielectrics for high voltage applications but they increase thermal stress.The two electrodes are connected to a power source, which can either be a direct current or alternating current power source. Figure 1.3 shows the typical configuration that was just described. Typically electrodes are made of copper or copper alloys due to their high conductivity and cost effectiveness, while the dielectric material can be chosen between Kapton, Teflon or polyamide, among others, due to their thermal stability and dielectric strength [20].

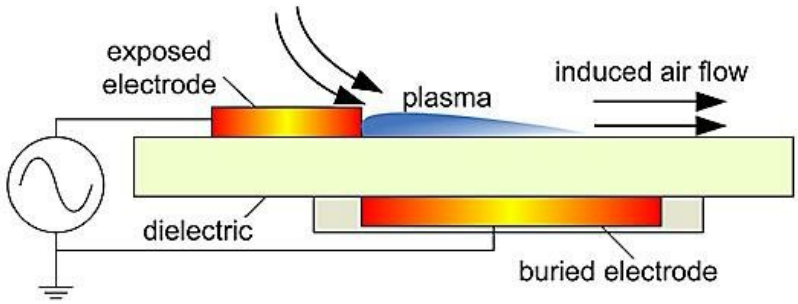

Figure 1.3: Scheme of a Dielectric Barrier Discharge Actuator [21]

When a high voltage is applied across the two electrodes, exceeding the value of the breakdown electric field E_b, the air above the insulated electrode ionizes creating a non-thermal plasma. The generated charged particles are accelerated by means of the electric field between the electrodes, inducing the so called ionic wind or electric wind and causing them to collide with the neutral particles in the air. Through these collisions, momentum is exchanged, which results in a net body force transmitted to the airflow, called electrohydrodynamic (EHD) force. This induces a wall jet-like flow in the air in the direction of the embedded electrode causing reattachment to the surface. However, unlike actual jet actuators, this induced flow does not entail mass injection.

Although to the eye the plasma is uniform, high-speed photographs have shown that the discharge is actually made up of many micro-discharges that are generated in discreet positions along the actuator [1].

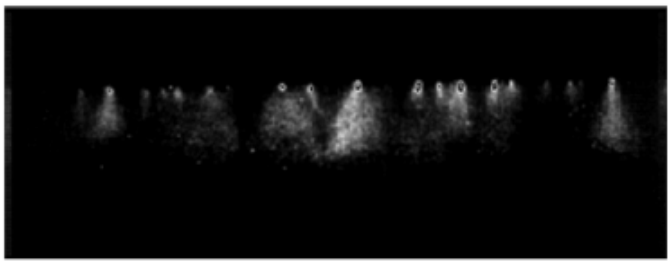

Figure 1.4: Micro-discharges

Two of the biggest advantages of DBDs are that the produced plasma is non-thermal, meaning that the discharge process described barely increases the temperature of airflow, and the fact that the discharge is self-limiting and stable at atmospheric pressure. This is thanks to the dielectric that stores negative electrical charges on its surface, thus quenching further plasma creation, unless the input voltage polarity is reversed. The asymmetrical nature of the actuator allows for a non-zero net force to be produced in the main direction of the flow. It has, notably, been demonstrated that when electrodes are asymmetrically placed, the wall jet velocity can reach values up to 7 m/s [22]. Furthermore, it was proven that induced velocity reaches an optimum value for a horizontal distance between the two electrodes of 5 mm [23], as shorter distances accelerate electrons less, while larger distances generate a weaker electric field.

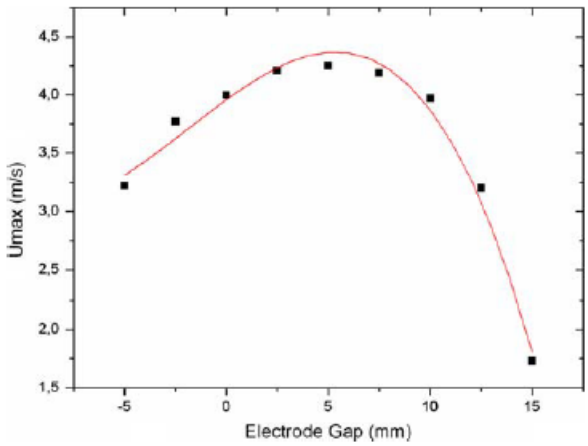

Figure 1.5: Evolution of induced velocity with gap between the two electrodes

It has also been found that there is an ideal position along the wing profile of these actuators for flow reattachment purposes. Through numerical simulations, it has been possible to confirm that the optimal DBD placement is at the leading

edge of the airfoil, because it results in the best aerodynamic efficiency possible at all angles of attack [24] as can be seen in Fig.1.6. At the same time, it has been proven that if the actuator is placed too far from the leading edge, it completely loses its effect on the airflow. This happens because the closer to the tip of the wing, the more momentum the boundary layer has and, therefore, the injection of energy from the actuator has a bigger effect on the flow.

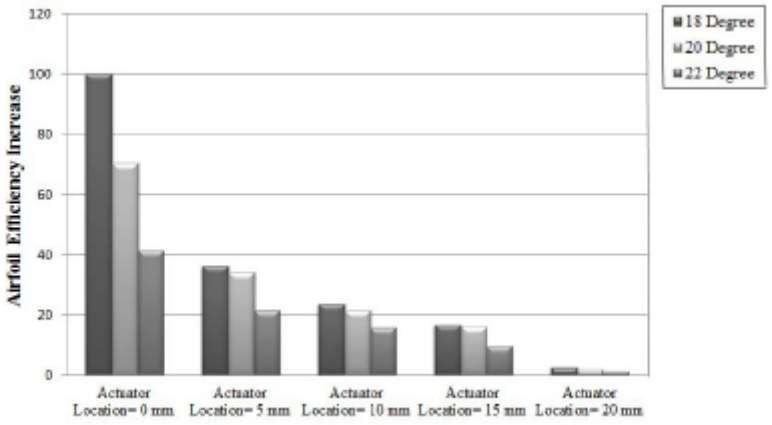

Figure 1.6: Evolution of efficiency with actuator's location at different angles of attack

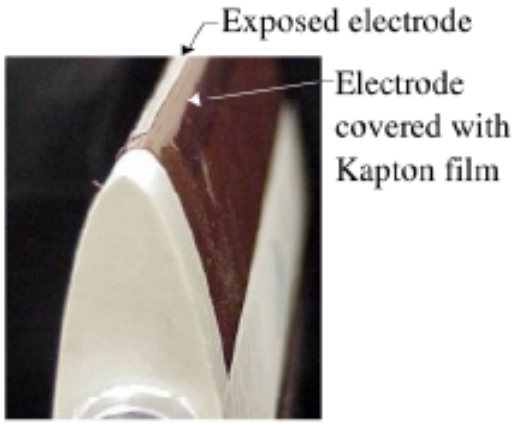

Figure 1.7: Leading-edge DBD

Working Parameters

Depending on the specific parameters chosen, as well as actuator geometry and voltage waveform (harmonic, sawtooth or square waveform) different plasma structures can arise. The most common ones are corona-like regimes, consisting of regions of non-neutral collection, and streamer-like regimes, non-neutral filaments which spread along with the flow. These structures in turn influence the coupling between plasma and the airflow changing the impact of the actuator on aerodynamics.

Electrode width influences plasma expansion along the surface: the wider the hidden electrode the farther the plasma can stretch leading to an increased induced velocity. This trend remains true only until a certain width is reached, after which the electric field along the electrode becomes too weak to pull the charged particles and plasma does not propagate further, regardless of electrode size. It has been proven, in fact, by Forte et al. that plasma extension is never larger than 2 cm [23].

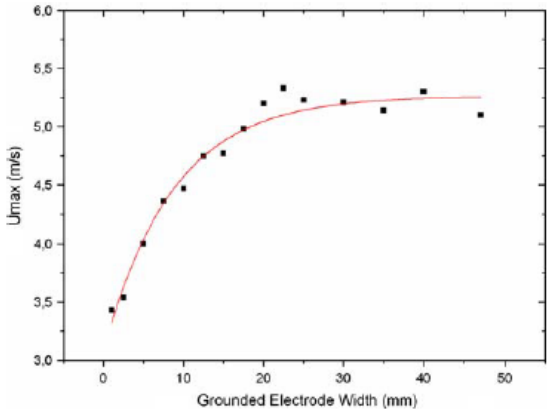

Figure 1.8: Evolution of induced velocity with grounded electrode width

Input frequency is also a very important factor: the higher the frequency, the more the air is ionized, and therefore the faster the ionic wind. Here, too, the velocity reaches a plateau above an optimum value, which varies depending on the case being considered [23]. Increasing the voltage amplitude would have the same result as with frequency, leading, however, to a much larger power consumption and higher costs. Also, it increases local heating that can damage heat sensitive structures near the actuator [20]. As can be seen in Fig. 1.9 increasing the frequency causes a surge in needed electrical power, but, the higher the voltage the faster this rise becomes.

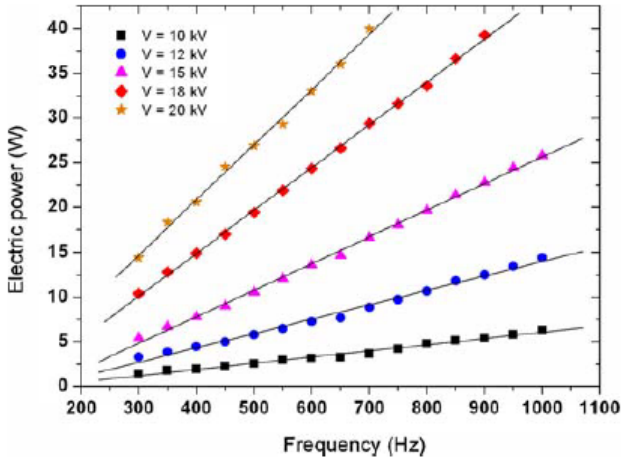

Figure 1.9: Evolution of electric power with frequency at different voltage values

As was said, both AC and DC operations are possible, with the former one being preferred due to its lower breakdown voltage [1] and to maintain discharge for longer time periods. The optimal solution, however, is to use a signal in the form of repetitive short pulses with DC bias [25]. The positive bias of the exposed electrode ensures gas motion away from the electrode and toward the dielectric, while the pulses are needed to replenish free electrons near the exposed electrode. This allows the formation of repetitive discharges increasing the actuation time. These pulses have very short life, 2-5 ns, as increasing their duration has been proven to decrease the actuator's efficiency.

Usual working parameters are frequencies between 1-20 kHz, though greater values (up to 100 kHz) have been applied successfully, and voltage amplitudes between 5-20 kV [26].

Modelling

DBD actuators can be modeled numerically with two different approaches: first-principles models or phenomenological models. The latter, also called simplified methods, are meant to study the bulk effects of the actuator on the flow field; they are, therefore, simpler and less computationally expensive, however they do not properly describe plasma behaviour. Among the most popular phenomenological methods are the Shyy model [27], the Orlov model [28], and the Suzen and Huang model [29]. The Shyy body force model assumes that the body force is independent of time and acts only in regions where the plasma is present [22] and that the electric field is linear in space: $\mathbf{E}(x, y) = E_0 - k_1 x - k_2 x$. E_0 represents the input voltage divided by the electrode gap.

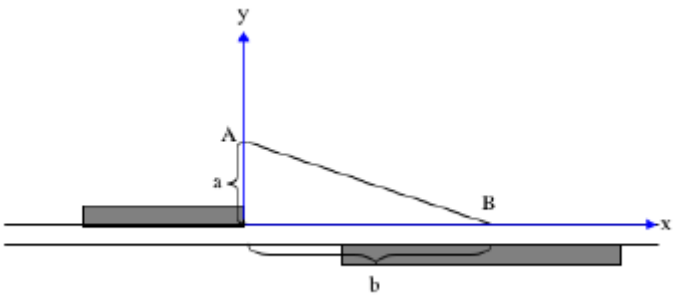

Figure 1.10: Scheme of the Shyy model

The Suzen-Huang approach defines a potential Φ that can be divided in two components ($\Phi = \phi + \varphi$), one given by the external electric field, ϕ, and the other, φ given by the net charge density inside the plasma [20]. These two potentials are then treated individually.

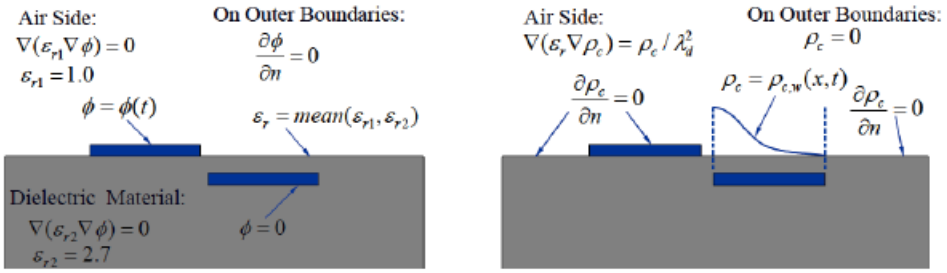

Figure 1.11: Classical governing equations and boundary conditions for Suzen and Huang model

The Orlov model, the most advanced of the three, is the only one to compute a time-dependent induced flow by solving differential equations with time-dependent boundary conditions. A modified version of the Suzen model, developed later in time, is also able to give time-dependent results. The main disadvantage of these models is that by not focusing on plasma physics they tend to produce underestimated results. For example, it was demonstrated in Ref. [30] that the Suzen-Huang scheme underestimated both the EHD force in the streamwise direction and the induced velocity. Also, these methods often require values of parameters that cannot be computed through the method itself but have to be later corrected through experimental results [31]. Therefore, they have a limited and non-universal applicability.

First-principles models, on the other hand, describe more accurately plasma discharge dynamics and species interactions. They require the solution of transport

equations for the various species considered along with a Poisson equation and the Navier-Stokes equations and are, therefore, more expensive from a computational standpoint, with computational times up to one order of magnitude greater than simplified models [32]. First-principles models can be classified as fluid, kinetic or hybrid models. All three of these methods require the solution of a Boltzmann Equation for electron velocity or energy distribution; kinetic models do this using Monte-Carlo methods, while fluid models assume a distribution function and a local thermodynamic equilibrium in the plasma. Hybrid models are a mix of both, combining the efficiency of fluid models and the accuracy of kinetic [33]. One of the most reliable and commonly used fluid models is Magneto-Fluid-Dynamics (MFD) which derives from the Magneto-Hydro-Dynamics (MHD) model, well established in the world of plasma physics that, as the name says, describes the motion of fluids under applied electric or magnetic fields [34]. This model was firstly developed by Resler and Sears who originated the idea that electromagnetic effects could be used to alter aerodynamic performance around sixty years ago, when they recognized that an applied Lorentz force could be used to accelerate or decelerate a gas [35]. This method has a very wide range of applications that are not limited to aeronautics, like astrophysics, to study plasma dynamics within and close to stars and geophysics, where it is used to analyze the effect of Earth's magnetic field on atmospheric flows.

Other less popular models exist, like the Lumped-Element Circuit Model which consists of representing the plasma bulk as an electrical circuit. More specifically, the domain is divided into parallel sub-circuits, each made up of two capacitors, representing, respectively, air and the dielectric, and two air resistors [1].

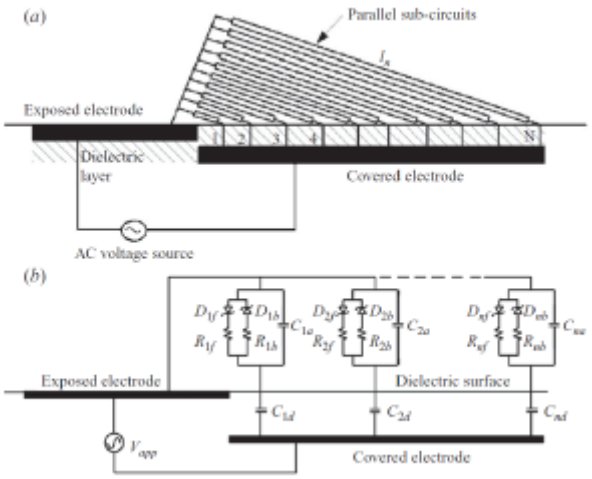

Figure 1.12: Scheme of the Lumped-Element Circuit Model

Other configurations

In the last decade, new configurations of DBD actuators have emerged; each of these consists in the combination of the classical DBD previously described and a different kind of flow control actuator. They use similar materials and have similar applications to those mentioned in Section 1.2, but they differ in geometry and positioning of the components.

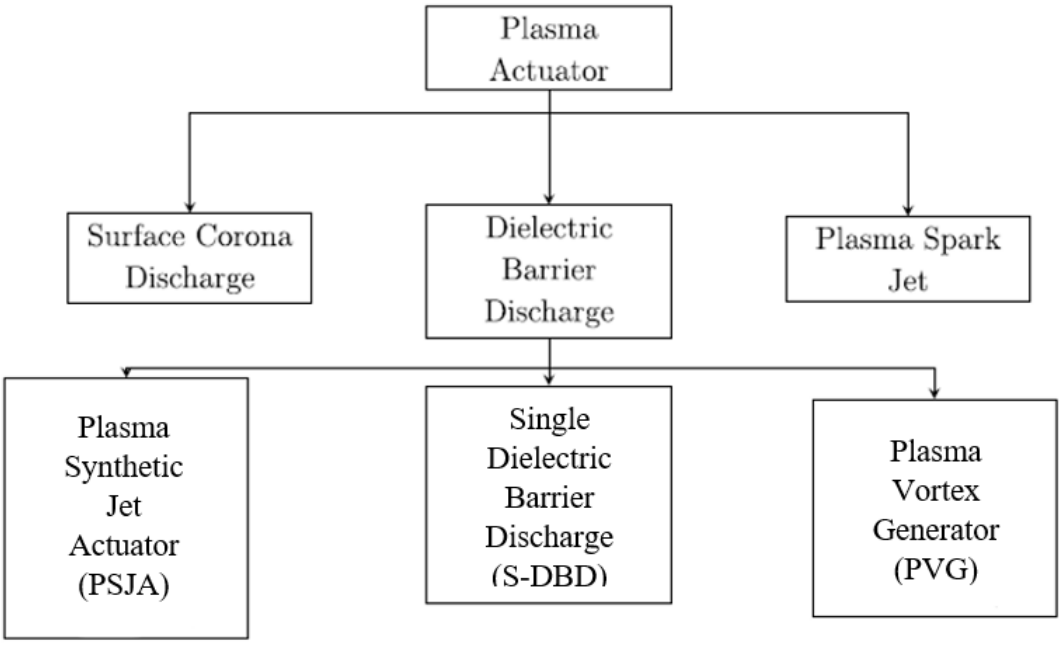

Figure 1.13: Types of Plasma Actuators

Plasma Synthetic Jets (PSJs) [36, 20] combine plasma discharges and synthetic jets to generate pulsating plasma jets, which improve flow control and separation delay compared to the classical configuration. They exist in two configurations: annular and linear jets. Annular jets are made up of an embedded annular electrode, an exposed electrode and a insulating (dielectric) sheet, while linear ones have two exposed electrodes and one or two embedded ones, along with the dielectric wall. In both configurations there is little to no gap between electrodes. There also is a so-called second generation PSJ which utilizes a third exposed electrode called trigger and a longer gap between electrodes. They function by pulling fluid close to the surface by the actuators and ejecting it back outside in the form of a jet, creating a vortical structure. Often, two or three PSJs can be used together, positioned in the spanwise direction.

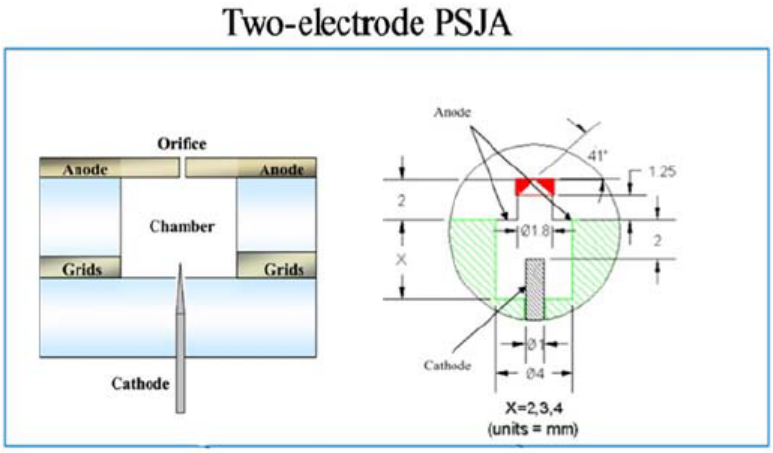

Figure 1.14: Scheme of a Plasma Synthetic Jet Actuator

Another configuration is the Plasma Vortex Generator (PVG) [36, 20, 37], which creates plasma vortexes with the goal of modifying flow structures, improving aerodynamic efficiency and enhancing mixing. Their working concept is the opposite of classical DBDs: they re-energize the boundary layer by bringing in high-momentum fluid from the outer flow. Vortexes are formed by a series of plasma actuators placed in the free stream direction; if the actuators are asymmetrically positioned, then co-rotating vortices are obtained, otherwise if the actuators are symmetrical with one common embedded electrode counter-rotating vortices are generated. Their effect is analogous to classical mechanical vortex generators, but unlike them, they do not cause additional drag on the airfoil.

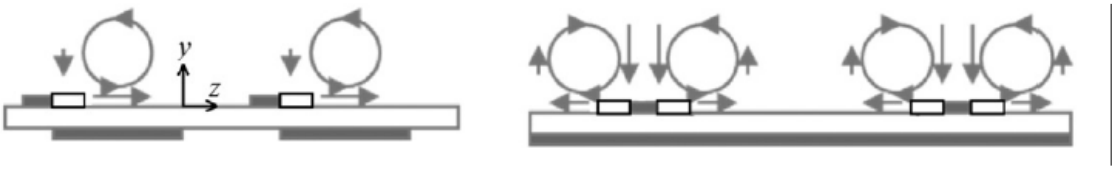

Figure 1.15: Co-rotating (left) and counter-rotating (right) PVGs

A third configuration is the Plasma Flap (PF), which is an integrated plasma actuator designed as a movable flap within an aircraft wing to actively control lift and drag [20]. If properly positioned they can even replace flaps (or slats), causing a reduction in weight and mechanical complexity [2]. For example, the so-called Plasma Gurney flap, is actually a DBD actuator which substitutes an actual Gurney flap.

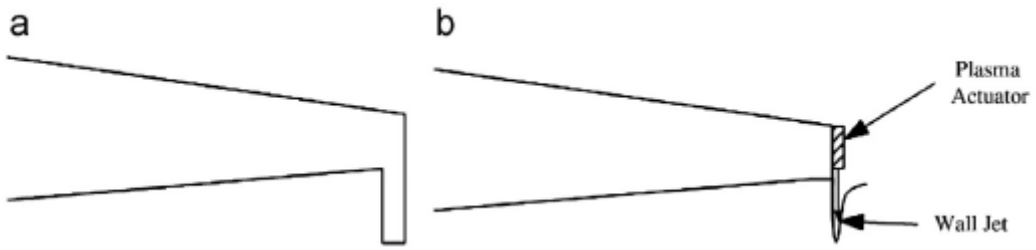

Figure 1.16: Regular Gurney flap (left) and Plasma Gurney flap (right)

Stair-shaped DBD actuators enhance induced velocity and plasma discharge extension without compromising actuator durability, horseshoe and serpentine actuators are particularly efficient in low-speed regions. Most of these configurations have the ability to influence all three directions of the airflow, while regular DBDs have mainly two-dimensional effects. However, they are more complex to realize and operate and are of newer development, which is why classic DBDs are the most utilized configuration.

1.3 Challenges and goals of this thesis

It is necessary to further study the interactions between plasma and airflow, as the phenomena taking place are not yet fully understood. A better understanding could lead to an improvement in power consumption, costs, and overall efficiency of the actuators. Most studies so far have considered dry air and medium-to-high Reynolds numbers, reproducing values typical of airplane flight. To further comprehension of this technology it is fundamental to study DBD operation at very low Reynolds numbers (Re $<$ 50,000), where viscous forces are dominant to inertial forces, altering boundary layer physics [38], and in humid air, as moisture is known to disrupt electrical discharges, making them more unstable, and degrade dielectric materials [39].

The goal of this thesis is to use the code developed by Arpa in [40] to study the behaviour of dielectric barrier plasma discharges under multiple working conditions. Different power supplies are considered, as well as different electrode configurations, switching from an exposed anode to an exposed cathode. Distinct chemical models are implemented, whose accuracy depends on the number of reactions and phenomena considered. The main interest is to understand how the discharge develops over time by analyzing the movement of charged particles and the distribution of electric potential in the computational volume. The second step consists in investigating the

effects that these discharges have on the external flow by computing the generated body force and Joule heating.

This thesis is divided into three sections. Chapter 2 describes the model used to represent plasma, complete with its physical and chemical aspects, Chapter 3 introduces the numerical scheme applied to solve such model, and Chapter 4 presents the obtained results.

Chapter 2

Physical and chemical model for DBD actuators

2.1 Fundamentals of DBD Modeling

Numerical simulations are fundamental for a deeper understanding of Dielectric Barrier Discharge actuators as they have unique benefits such as being able to replicate parameters that are hard to measure experimentally and can achieve higher resolutions. Plasma is particularly complex to model from a physical and chemical point of view as it is made up of multiple species and involves several chemical reactions; a nitrogen-oxygen mixture at atmospheric pressure contains around 25 species and involves more than 400 reactions [41]. A small part of these reactions, those involving only oxygen are shown in Figure 2.1. A computational model needs to describe the nature of plasma accurately enough in order to produce satisfying results, but, to avoid excessive computational costs and times, approximations are needed.

e	+	$2O_2$	$\longrightarrow$	O_4^+	+	$2e$	ionization (O_2+$O_2^+ \rightarrow O_4^+$)
e	+	O_2	$\longrightarrow$	O^-	+	O	dissociative attachment
e	+	O_2	$\longrightarrow$	O_2^+	+	e	meta-stable excitation
e	+	O_2	$\longrightarrow$	$2O$	+	e	dissociation
e	+	O_4^+	$\longrightarrow$	$2O_2$			dissociative recombination (glow)
O_4^+	+	O_2	$\longrightarrow$	O_4^+	+	O_2	momentum transfer
O^-	+	O_2	$\longrightarrow$	O^-	+	O_2	momentum transfer
O^-	+	O_4^+	$\longrightarrow$	$2O_2$	+	O	recombination

Figure 2.1: All oxygen reactions [42]

As previously mentioned, among the first-principles fluid models, one of the most reliable is the MFD model, which consists in coupling one continuity equation for each constitutive species with the conservation equations for global mass, momentum and energy:

$$\frac{\partial \rho_i}{\partial t} + \nabla \cdot \rho_i \mathbf{v} = -\nabla \cdot \mathbf{J}_{m,i} + \Omega^i_{ch}, \qquad i = 1, ...N-1 \tag{2.1}$$

$$\frac{\partial \rho}{\partial t} + \nabla \cdot \rho \mathbf{v} = 0 \tag{2.2}$$

$$\frac{\partial (\rho \mathbf{v})}{\partial t} + \nabla \cdot \rho \mathbf{v}\mathbf{v} = \nabla \cdot \tau + \rho_c \mathbf{E} + \mathbf{j} \times \mathbf{B} \tag{2.3}$$

$$\frac{\partial (\rho q_e)}{\partial t} + \nabla \cdot [(\rho q_e + p)\mathbf{v}] = -\nabla \cdot (\mathbf{J}_u - \tau \cdot \mathbf{v}) + \mathbf{j} \cdot \mathbf{E} \tag{2.4}$$

where $q_e = 1.602 \cdot 10^{-19}\, C$ is the elementary charge, m_i and q_i are the molecular mass and charge of the i-th species, $\mathbf{J}_{m,i}$ and $\mathbf{J}_u$ are the mass and internal energy diffusive fluxes, while N is the total number of constitutive species. $\mathbf{j}$ is the total current, defined as:

$$\mathbf{j} = \rho_c \mathbf{v} + \sum_{i=1}^{N} q_i \mathbf{J}_{m,i} \tag{2.5}$$

The chemical production term Ω^i_{ch} can be obtained by applying the so-called law of mass action to every chemical reaction considered. $\mathbf{E}$ and $\mathbf{B}$ are the electric and magnetic fields, respectively, which can be calculated by solving Maxwell's equations:

$$-\epsilon_0 \frac{\partial \mathbf{E}}{\partial t} + \epsilon_0 c^2 \nabla \times \mathbf{B} = \mathbf{j} \tag{2.6}$$

$$\frac{\partial \mathbf{B}}{\partial t} + \nabla \times \mathbf{E} = 0 \tag{2.7}$$

$$\nabla \cdot \mathbf{B} = 0 \tag{2.8}$$

$$\nabla \cdot \epsilon_0 \mathbf{E} = \rho_c \tag{2.9}$$

with c being the speed of light and $\epsilon_0 = 8.854 \cdot 10^{-12}\, \frac{F}{m}$ the vacuum permittivity. When a physical medium is considered, new terms appear in these equations: polarization $\mathbf{P}$ and magnetization $\mathbf{M}$; in a gas, however, these terms are so small that they are considered negligible, this is called a vacuum approximation.

Only N-1 continuity equations are needed, as the Nth equation can be replaced by an equation for global density:

$$\rho = \sum_{i=1}^{N} \rho_i \tag{2.10}$$

The global charge density is defined as:

$$\rho_c = \sum_{i=1}^{N} q_i \frac{\rho_i}{m_i} \tag{2.11}$$

and its conservation equation is:

$$\frac{\partial \rho_c}{\partial t} + \nabla \cdot \mathbf{j} = 0 \tag{2.12}$$

The main difference between MFD and the more general MHD approach is the fact that the former takes into account plasma features such as the effect of displacement current, identified by the term $\epsilon_0 \frac{\partial \mathbf{E}}{\partial t}$, and the formation of a space-charge separation zone known as a plasma sheath. A plasma sheath is a near-wall layer of plasma of the scale of a few Debye lengths[1] enclosing a large number of positive ions which is subject to high temperature, velocity, and density gradients. Both mentioned mechanisms are fundamental in the development of the discharge and therefore should be considered.

The first main simplification is due to the fact that plasma temporal scales (in the order of microseconds to nanoseconds) are much smaller than those of gas dynamics. The effects of the main flow field can therefore be neglected, treating the plasma as if it evolved in a background frozen flow field. Thanks to this the problem can be separated into two parts: the first one consists in solving plasma dynamics, specifically equations (2.1) and (2.6 - 2.9), while the second one consists in coupling the plasma with the external flow, using the previously computed body force and electromagnetic parameters as source terms in the remaining conservation equations (2.2, 2.3). This approximation is only valid if plasma control is applied for time periods similar to the time scales of fluid dynamics, otherwise the external flow field greatly influences plasma dynamics and the two problems can no longer be separated.

[1]Debye length $\lambda_D = \sqrt{\frac{\epsilon_0 k_b T_e}{n_e q_e^2}}$ is a measure of the distance at which charged particles shield the Coulomb effect of another, oppositely charged particle [43].

2.2 Plasma physics

Drift-Diffusion Approximation

In order to capture the essentials of plasma behaviour without excessively complicating the model, a four-species plasma is typically considered, made up of positive ions, negative ions, electrons, and neutral particles.

Due to the fast diffusion speed of charged particles, the mixture can be considered at rest ($\mathbf{v} = 0$), resulting in a simplified version of the continuity equation and the total current:

$$\frac{\partial \rho_i}{\partial t} = -\nabla \cdot \mathbf{J}_{m,i} + \Omega^i_{ch} \tag{2.13}$$

$$\mathbf{j} = \sum_{i=1}^{N} q_i \mathbf{J}_{m,i} \tag{2.14}$$

Since the speeds of charged particles are much lower than relativistic velocities [44], the charges in the plasma are assumed to have enough time to redistribute themselves [17] following the Boltzmann distribution. This, paired with the absence of an external magnetic field, makes it possible to neglect the magnetic field and its variation in time ($\mathbf{B} = \frac{\partial \mathbf{B}}{\partial t} = 0$). Faraday's law, therefore, becomes $\nabla \times \mathbf{E} = 0$, meaning that the electric field is conservative and that it can be expressed as the gradient of a scalar potential: $\mathbf{E} = -\nabla\Phi$. Introducing this expression in Gauss' law, a Poisson equation for electric field is obtained:

$$\nabla \cdot \epsilon_r \nabla\Phi = \frac{\rho_c}{\epsilon_0} \tag{2.15}$$

where ϵ_r is the relative dielectric permittivity, described as the ability of a material, in this case the dielectric barrier, to store electrical energy in the presence of an electric field [45].

Due to the fast time scales of discharges, only small variations of ions and neutrals temperatures are expected, small enough that they do not influence particles dynamics; their temperatures are therefore considered constant and equal to that of gas temperature. The only exception is electrons, whose temperature changes throughout the process due to variations in the electric field. When approaching the wall it is expected that electrons lose some energy due to them interacting with the wall, however, since there is not a predefined model to evaluate this change in temperature, it's assumed that electrons thermalize instantaneously at the same temperature of heavy particles when along the wall.

To define diffusive fluxes, a Drift-Diffusion approximation is used [46], in which

diffusion is driven only by mass concentration gradients and the electric field:

$$\mathbf{J}_{m,+} = -D_+ \nabla \rho_+ + \mu_+ \rho_+ \mathbf{E} \tag{2.16}$$

$$\mathbf{J}_{m,-} = -D_- \nabla \rho_- - \mu_- \rho_- \mathbf{E} \tag{2.17}$$

$$\mathbf{J}_{m,e} = -D_e \nabla \rho_e - \mu_e \rho_e \mathbf{E} - D_e \rho_e \frac{\nabla T_e}{T_e} \tag{2.18}$$

$$\mathbf{J}_{m,n} = -D_n \nabla \rho_n \tag{2.19}$$

where e, $+$, $-$ and n refer, respectively, to electrons, positive ions, negative ions, and neutral particles, D_i are the diffusion coefficients, and μ_i are the mobilities of the constitutive species. The product between species mobility and the electric field defines the drift velocity of that species:

$$v_{dr,i} = \mu_i \mathbf{E} \tag{2.20}$$

This model represents a good compromise between the simplicity desired for the model and physical accuracy; it was demonstrated to be a good approximation in a pressure range of 1-50 torr and with voltage drops between 0.3 and 10 kV. The main advantage of this approach is that it is able to simulate a time-varying body force, when many other models, especially phenomenological ones, only provide a time-averaged force.

Local Field Approximation

Discharge ionization is mainly the result of impacts between highly energized electrons and neutral particles, therefore, an equation for electron energy relaxation needs to be solved alongside the previously defined equations. Electron energy strongly influences chemical processes and transport properties. In fact, the different processes that happen in discharge formation, which will later be described in Chapter 2.3, are only activated when electrons reach a certain amount of energy. On the other hand, ion energy has little to no effect on the chemical processes and therefore an appropriate equation is not necessary. A macroscopic description of electron relaxation energy is not possible for discharge problems [40] because the electron equilibrium cannot be considered Maxwellian under strong applied electric fields. This is because in a plasma the mean free paths of particles are oftentimes larger than the plasma's macroscopic length scales causing distribution functions to differ from their Maxwellian forms [43]. Transport properties and chemical coefficients depend on a distribution function, the electron energy distribution function (EEDF), in the energy space: $f(\mathbf{x}, t, \epsilon)$. This function changes with the degree of ionization of the discharge and the waveform of the applied voltage among other parameters, and it can be calculated by solving the Boltzmann Equation

(BE):

$$\frac{\partial f}{\partial t} + \mathbf{v} \cdot \nabla f - \frac{q_e}{m_e} \mathbf{E} \cdot \nabla_V f = \mathbf{C}[f] \tag{2.21}$$

where $m_e \simeq 9.11 \cdot 10^{-31}\ kg$ is the mass of the electron, ∇_V is the velocity gradient operator, and $\mathbf{C}$ is the rate of change in f due to collisions.

In highly collisional discharges, like the ones considered in this thesis, typical electron energy relaxation times values are of the order of magnitude of $10^{-13}\ s$ to $10^{-9}\ s$, much smaller than the time scales of the discharges themselves. Therefore, it is possible to consider a decoupling between discharge dynamics and electron relaxation; this means that transport properties and chemical coefficients depend only on the local reduced electric field E/N, where N represents the total number density of particles. This approach is known as Local Field Approximation (LFA): it assumes an instantaneous balance between energy loss and particle acceleration in collisions between electrons and neutrals, and it eliminates the need for the electron relaxation equation previously mentioned [47]. At particularly low densities, which are not addressed in this thesis, the LFA says that parameters depend only on the ratio between electric field and field oscillation frequency E/ω instead of E/N. Mean electron energy and electron mobility can, in fact, be obtained through the resolution of the Boltzmann Equation, considering steady-state solutions only under the hypothesis of a uniform electric field and uniform cross sections. These assumptions are valid as long as a sufficiently refined grid is used.

When treating high-frequency (of the order of GHz) simulations, such as those later described in Chapter 4, variations in the electric field can be faster than electron energy relaxation, thus causing the LFA to become invalid. However, in order to keep the model relatively simple, in this thesis the approximation will be considered valid in all the case studies.

A second existing model, similar to the LFA is the Local Energy Approximation (LEA). This approach is not considered in this thesis, but is here briefly described for completeness. Under the LEA, rate coefficients are derived from the local value of the mean electron energy. In this case, the equation for electron energy must be included and solved. Generally, the LEA provides more accurate results than the LFA due to the temporal effects introduced by the electron energy equation, which are otherwise absent. However, models employing the LEA tend to be more computationally expensive as the treatment of electron collision and heating terms can lead to numerical stiffness.

Transport properties

As previously stated, transport properties depend only on the local electric field because of the LFA model. Particle mobility defines how quickly said particle moves in a fluid when accelerated by an electric field; here, in order to simplify the model, ion mobilities are considered identical and are evaluated from empirical formulas:

$$\mu_{+,-} = \frac{2100}{p} \quad \left[\frac{cm^2}{V \cdot s}\right] \qquad if \quad \frac{E}{p} < 39.3 \quad \frac{V}{cm \cdot torr} \tag{2.22}$$

$$\mu_{+,-} = \frac{14750}{p\sqrt{E/p}} \quad \left[\frac{cm^2}{V \cdot s}\right] \qquad if \quad \frac{E}{p} > 39.3 \quad \frac{V}{cm \cdot torr} \tag{2.23}$$

where all pressures are expressed in torr. Electron mobilities are, instead, consistently obtained by utilizing a BE solver called Bolsig+ [48].

The diffusion coefficient, on the other hand, relates the flux due to molecular diffusion to the concentration gradient, through Fick's law:

$$F_i = -D_i \nabla n \tag{2.24}$$

The diffusion coefficient of the i-th species is connected to the mobility of that same species through Einstein's relation, in the so-called Einstein-Smoluchowski formulation for charged particles:

$$D_i = \frac{\mu_i k_b T_i}{q_e} \quad \left[\frac{m^2}{s}\right] \tag{2.25}$$

where $k_b = 1.38 \cdot 10^{-23}\ \frac{J}{K}$ is Boltzmann's constant.

2.3 Plasma chemistry

The chemical model considered is an ideal nitrogen-oxygen mixture, made up of four species: electrons, positive ions (an averaged concentration of N_2^+ and O_2^+), negative ions (O_2^-, O^-), and neutrals (N_2, O_2, O), at atmospheric pressure and room temperature. Electrodes are considered to be powered by high frequency voltages, of the order of MHz or GHz, in order to provide sufficient power input to overcome the creation of negative ions that happens in electronegative gasses, which cause a reduction of the generated body force on neutrals.

In general, two different phases can be distinguished in the process of discharge formation: a triggering phase, where the plasma is formed, and a sustaining phase, that starts once equilibrium between drift of charged particles, electric field relaxation and mass production is reached. A vast number of chemical reactions occur in both phases, thus a more or less accurate chemical model can be obtained depending on which processes are considered and which are excluded.

Avalanche ionization

The main process of formation of positive ions is primary avalanche ionization, where free electrons, also known as seed electrons, impact with neutrals forming positive ions and new electrons, which in turn impact with neutrals, giving start to an exponential production (thus the name avalanche) of charged particles. The reactions that describe primary ionization are:

$$N_2 + e^- \rightarrow N_2^+ + 2e^- \tag{2.26}$$
$$O_2 + e^- \rightarrow O_2^+ + 2e^- \tag{2.27}$$

These reactions are triggered when the local electron energy reaches values of $T_e \simeq 13eV$ for oxygen and $T_e \simeq 15eV$ for nitrogen. The correlated production rate is evaluated as:

$$S_{ion} = \nu_i \frac{\rho_e}{m_e} \tag{2.28}$$

where ν_i is the primary ionization frequency, which can be expressed as a product of the electron drift velocity $v_{dr,e}$ and Townsend's first ionization coefficient α, which represents the number of ions generated per unit length. Townsend's coefficient can be calculated, under the Local Field Approximation, as a function of the local electric field, using empirical equations like those in Ref. [49]:

$$\alpha = \begin{cases} \frac{1}{\theta\mu_e}\left(10^{-8.25}\cdot 10^{-\frac{365}{\theta}}\right) \quad cm^{-1} & if \;\; 3 \leq \theta \leq 30 \\ 1.17\cdot 10^{-4}\cdot p\left(\frac{E}{p} - 32.2\right)^2 \quad cm^{-1} & if \;\; 44 \leq \frac{E}{p} \leq 176 \\ 15p\cdot exp\left[-\frac{365}{E/p}\right] \quad cm^{-1} & if \;\; 100 \leq \frac{E}{p} \leq 800 \end{cases} \tag{2.29}$$

where $\theta = \frac{E}{N}\cdot 10^{-17}\; V\cdot cm^2$ and all pressures are expressed in torr. Their forward reaction rates can be obtained from the following formulas:

$$\log(k_{O_2}) = -8.3 - \frac{36.5}{\theta} \tag{2.30}$$
$$\log(k_{N_2}) = -8.8 - \frac{28.1}{\theta} \tag{2.31}$$

Another possible equation to compute Townsend's coefficient is:

$$\frac{\alpha}{p} = 39.11exp\left[\frac{-1.068\cdot 10^2}{(dE/dp)^{0.69}}\right] \tag{2.32}$$

Attachment reactions

During the discharge, some processes that cause the loss of free electrons happen through reactions of attachment to neutrals, generating negative ions, as was mentioned at the beginning of the chapter. Among these, the most relevant is the three-body attachment reaction, which, as the name says, involves three particles, two neutrals, and an electron:

$$e^- + 2O_2 \rightarrow O_2^- + O_2 \tag{2.33}$$
$$e^- + O_2 + N_2 \rightarrow O_2^- + N_2 \tag{2.34}$$

The rates of these two reactions are dependent on the electric field, so most of the production of negative ions occurs during low applied voltages.

$$k_{a1} = 1.4 \cdot 10^{-29} \left(\frac{300}{T_e}\right) exp\left(-\frac{600}{T_h}\right) exp\left(\frac{700(T_e - T_h)}{T_e \cdot T_h}\right) \quad \left[\frac{cm^6}{s}\right] \tag{2.35}$$
$$k_{a2} = 1.07 \cdot 10^{-31} \left(\frac{300}{T_e}\right)^2 exp\left(-\frac{70}{T_h}\right) exp\left(\frac{1500(T_e - T_h)}{T_e \cdot T_h}\right) \quad \left[\frac{cm^6}{s}\right] \tag{2.36}$$

with the temperatures expressed in Kelvin. The related decay rate of electrons and the attachment frequency can be calculated as:

$$S_{att} = \nu_{att} \cdot \frac{\rho_e}{m_e} \tag{2.37}$$
$$\nu_{att} = k_{a1} N_{O_2}^2 + k_{a2} N_{N_2} N_{O_2} \tag{2.38}$$

Another process that causes the decay in number electron density is dissociative attachment reactions:

$$e^- + O_2 \rightarrow O^- + O \tag{2.39}$$

These reactions are triggered at $T \simeq 10eV$, a value similar to those of electron ionization reactions, and its frequency reaches maximum values lower than those of the previously mentioned three-body processes. The values of dissociative attachment frequency $\nu_{att,d}$ is obtained from the Bolsig+ solver, while the reaction rate is:

$$\log(k_{att,d}) = \begin{cases} -9.3 - \frac{12.3}{\theta} & if \ \ \theta < 8 \\ -10.2 - \frac{5.7}{\theta} & if \ \ \theta > 8 \end{cases} \tag{2.40}$$

Recombination reactions

Ulterior processes that take place in the plasma bulk are recombining processes, which are slower than those discussed so far, but they have been proven to influence the life duration of the discharge. Among the most important, there are two-body negative ion-positive ion recombination:

$$A^- + B^+ \rightarrow A + B \tag{2.41}$$

$$k_{rec} = 2 \cdot 10^{-7} \cdot \left(\frac{300}{T_h}\right)^{0.5} \quad \left[\frac{cm^3}{s}\right] \tag{2.42}$$

where A^- represents a generic negative ion and B^+ a generic positive ion, while M represents neutrals. Three-body negative ion-positive ion recombination:

$$A^- + B^+ + M \rightarrow A + B + M \tag{2.43}$$

and dissociative ion-electron recombination:

$$N_2^+ + e^- \rightarrow 2N \tag{2.44}$$

$$O_2^+ + e^- \rightarrow 2O \tag{2.45}$$

whose reaction rates can be approximately obtained as:

$$k_{N_2,rec} = 2.8 \cdot 10^{-7} \cdot \left(\frac{300}{T_e}\right)^{0.5} \tag{2.46}$$

$$k_{O_2,rec} = 2 \cdot 10^{-7} \cdot \left(\frac{300}{T_e}\right)^{0.5} \tag{2.47}$$

The recombination rates for equations 2.41 and 2.44-2.45 are, in this order:

$$S_{ii,rec} = \beta_{ii} \frac{\rho_+ + \rho_-}{m_+ + m_-} \tag{2.48}$$

$$S_{ie,rec} = \beta_{ie} \frac{\rho_+ + \rho_e}{m_+ + m_e} \tag{2.49}$$

where the two parameters β_{ii} and β_{ie} are called rate coefficients:

$$\beta_{ii} = 2 \cdot 10^{-7} \left(\frac{300}{T_h}\right)^{0.5} \cdot \left[1 + 1 \cdot 10^{-18} N \left(\frac{300}{T_h}\right)^2\right] \quad \left[\frac{cm^3}{s}\right] \tag{2.50}$$

$$\beta_{ie} = 2 \cdot 10^{-7} \left(\frac{300}{T_e}\right)^{0.5} \quad \left[\frac{cm^3}{s}\right] \tag{2.51}$$

Electron detachment

Finally, the last process considered in the model is the detachment of electrons from negative oxygen ions:

$$O_2^- + O_2 \rightarrow 2O_2 + e^- \tag{2.52}$$

whose forward rate constant and detachment rate are expressed, relatively, as:

$$k_{dO_2} = 8.6 \cdot 10^{-10} exp\left(-\frac{6030}{T_h}\right)\left[1 - exp\left(-\frac{1570}{T_h}\right)\right] \quad \left[\frac{cm^3}{s}\right] \tag{2.53}$$

$$S_{dO_2} = \nu_{dO_2}\frac{\rho_-}{m_-} \tag{2.54}$$

with the detachment frequency defined as $\nu_{dO_2} = k_{dO_2} N_{O_2}$.

Further reactions, involving other ions like N_4^+, are not considered to preserve the simplicity of the model. Also, electronic states of the particles are not considered, as a majority of them are very short lived with respect to the processes taking place, thus not playing a role in the described reactions [41].

Photoionization

Another very important process taking place during the discharge is photo-ionization. In the plasma photons are emitted through ultraviolet radiation, when these photons collide with neutrals or ions one or more electrons can be ejected in what is basically an ionization reaction. Photo-ionization plays a fundamental role in discharge development as it is responsible for most of the seed electrons present in the external flow that allow avalanche ionization to take place in the beginning phase of the discharge. Also, in the case of streamer discharges, it provides electrons near the streamer head which are necessary for streamer propagation. This process is not directly considered as to not further complicate the model, but due to its importance, it cannot be fully neglected. In its place, an artificial ionization term is utilized, called background density, which has the role to represent the free electrons that would be present due to photo-ionization. This corresponds to only considering the effects that this process would have on the plasma without the added complexity of having to model it. This is, however, a strong approximation as the artificial term is not quite able to properly simulate the actual phenomenon of photo-ionization. This results only in a correct qualitative description, while the quantitative results obtained for propagation length and velocity are approximate.

2.4 Boundary conditions

It is also necessary to define boundary conditions for the plasma model. Near walls, due to the strong electric field that develops in the sheaths, drift terms for both electron and ion diffusive fluxes are greater than diffusion due to mass concentration gradients, which is therefore neglected. Diffusive fluxes near the dielectric wall can therefore be expressed as follows:

$$\mathbf{J}_{m,+} = \mu_+ \rho_+ \mathbf{E}_{wall} \tag{2.55}$$

$$\mathbf{J}_{m,-} = -\mu_- \rho_- \mathbf{E}_{wall} \tag{2.56}$$

$$\mathbf{J}_{m,e} = -\mu_e \rho_e \mathbf{E}_{wall} - D_e \rho_e \frac{\nabla T_e}{T_e} \tag{2.57}$$

At walls, fluxes for charged particles have to be null, and at the cathode or cathode-like walls[2] secondary electron emission must be implemented. This process consists in the emission of so-called secondary electrons from the cathode (or cathode-like walls) due to the impact of positive ions on said walls. It is described by a parameter, the secondary electron emission coefficient γ, which is defined as the number of ejected electrons with respect to the number of impacting ions. It typically takes on small values, between 0.001 and 0.1, depending on the material and the nature of the wall that is being considered. Secondary emission is a fundamental process for the discharge as it allows the spreading of plasma along the dielectric. Everywhere else, a null gradient of charged particles is enforced.

$$\mathbf{J}_{m,+}^{anode} = 0 \tag{2.58}$$

$$\mathbf{J}_{m,-}^{cathode} = 0 \tag{2.59}$$

$$\mathbf{J}_{m,e}^{cathode} = -\gamma \mathbf{J}_{m,+}^{cathode} \tag{2.60}$$

$$\nabla \rho_{i,wall} = 0 \quad everywhere\ else \tag{2.61}$$

Boundary conditions for the electric potential at the electrodes are determined based of the imposed voltage. At other boundaries, electric potential is imposed as null. At the gas-dielectric interface, the boundary condition is obtained from:

$$\mathbf{E}_{gas,wall} - \epsilon_r \mathbf{E}_{diel,wall} = \frac{\sigma}{\epsilon_0} \tag{2.62}$$

where σ is the surface charge density, which is zero everywhere except on the dielectric surface where the charges accumulate. This density can, in turn, be

[2] A cathode-like wall is a surface that due to having a higher voltage than the electrode, it attracts negative charges, thus acting like a cathode. An example of this is when the exposed electrode acts as the anode and the dielectric has therefore the role of a cathode.

computed through the integration of the following equation:

$$\frac{\partial \sigma}{\partial t} = \left[\left(\mu_+ \frac{\rho_+}{m_+} + \mu_- \frac{\rho_-}{m_-} + \mu_e \frac{\rho_e}{m_e} \right) \mathbf{E} \cdot \mathbf{n} + D_e \frac{\rho_e}{m_e} \frac{\nabla T_e}{T_e} \cdot \mathbf{n} \right]_{wall} \tag{2.63}$$

where $\mathbf{n}$ is the normal to the dielectric wall. Zero charged particles density is considered inside the dielectric barrier.

2.5 Final outline of governing equations

Combining the physical and chemical models with the boundary conditions described in the previous sections (2.1,2.2,2.3) the final form of the governing equations is obtained:

$$\frac{\partial n_+}{\partial t} + \nabla \cdot \Gamma_+ = \alpha ||\Gamma_e|| - \beta_{ie} n_+ n_e - \beta_{ii} n_+ n_- \tag{2.64}$$

$$\frac{\partial n_-}{\partial t} + \nabla \cdot \Gamma_- = (\nu_{att} + \nu_{att,d}) n_e - \nu_{dO_2} n_- - \beta_{ii} n_+ n_- \tag{2.65}$$

$$\frac{\partial n_e}{\partial t} + \nabla \cdot \Gamma_e = \alpha ||\Gamma_e|| + \nu_{dO_2} n_- - \beta_{ie} n_+ n_e - (\nu_{att} + \nu_{att,d}) n_e \tag{2.66}$$

$$\epsilon_0 \nabla \cdot \epsilon_r \nabla \Phi = - \rho_c - \delta_s \cdot \sigma \tag{2.67}$$

$$\frac{\partial \rho}{\partial t} = 0 \tag{2.68}$$

$$\rho = \sum_i^{N_i} \rho_i \tag{2.69}$$

where δ_s is the Dirac delta which is non-zero only at the gas-dielectric interface and N_i is the number of species considered. The fluxes Γ_i are derived from the diffusive fluxes as:

$$\Gamma_i = \frac{\mathbf{J}_{m,i}}{m_i} \quad where\, i = +, -, e \tag{2.70}$$

while the number densities are derived from the densities:

$$n_i = \frac{\rho_i}{m_i} \tag{2.71}$$

Therefore, the equation for surface density becomes:

$$\frac{\partial \sigma}{\partial t} = [(\Gamma_+ - \Gamma_- - \Gamma_e) \cdot \mathbf{n}]_{wall} \tag{2.72}$$

At the walls, the fluxes are written as:

$$\Gamma_i = \pm \mu_i n_i \mathbf{E}_{wall} + \frac{1}{4} n_i v_{th,i} \tag{2.73}$$

where $v_{th,i}$ is the averaged thermal velocity of the i-th species, defined as:

$$v_{th,i} = \sqrt{\frac{8k_b T_i}{\pi m_i}} \tag{2.74}$$

Using these expressions, the same boundary conditions previously described can be implemented.

Once these equations have been solved, the body force and Joule heating can be calculated to be introduced as inputs into the conservation equations defined in Chapter 2.1:

$$\mathbf{F} = \rho_c \mathbf{E} = q_e(n_+ - n_- - n_e)\mathbf{E} \tag{2.75}$$

$$Q = \mathbf{J}_Q \cdot \mathbf{E} = q_e(\Gamma_+ - \Gamma_- - \Gamma_e) \cdot \mathbf{E} \tag{2.76}$$

Chapter 3

Numerical scheme

The biggest challenge in creating a numerical scheme for DBD actuators is the variety of spatial scales, from micrometers up to millimeters and possibly even centimeters, and very small temporal scales, orders of magnitude smaller than those of fluid dynamics. A scheme able to properly capture all of these different spatial and time scales is needed, operating within not too high computational times.

In discharge plasmas, it is possible to define four significant time scales, each representing a specific phenomenon. The dielectric relaxation time, also called Maxwell time, which takes into account the relaxation of the electric field, is defined as the maximum amount of time during which the field varies once a perturbation in charge density is applied:

$$\tau_{rel} = \frac{\epsilon_0}{q_e(\mu_+ n_+ + \mu_- n_- + \mu_e n_e)} \tag{3.1}$$

The drift time represents the typical evolution time of electrons, which are the fastest of charged particles, in an applied electric field:

$$\tau_{dr} = \frac{\lambda_D}{\mu_e ||\mathbf{E}||} \tag{3.2}$$

where λ_D is the previously defined Debye length. The last two temporal scales, which are representative of ionization and plasma decay, are relatively known as ionization time and decay time:

$$\tau_{ion} = \frac{1}{\alpha \mu_e ||\mathbf{E}||} \tag{3.3}$$

$$\tau_{dec} = \frac{1}{\nu_{att} + \nu_{att,d}} \tag{3.4}$$

In a plasma with a number electron density of $n_e \simeq 10^{18} - 10^{21}\ m^{-3}$, the relaxation time takes on values within the range $\tau_{rel} = 10^{-12} - 10^{-9}\ s$. If, on top of this, the

applied voltage is around $3-4\,kV$, then the electron drift velocity is of the order of magnitude of $10^4 - 10^5\,\frac{m}{s}$ and the Debye length $\lambda_D \simeq 10^{-6} - 10^{-5}\,m$, meaning the drift time can be expected to be of $\tau_{dr} = 5 \cdot 10^{-11} - 10^{-9}\,s$. In the bulk, however, away from the sheaths, the drift time is defined by the Courant-Friedrichs-Lewy (CFL) condition $\Delta t \leq \frac{\Delta x}{\mu_e ||\mathbf{E}||}$. At atmospheric pressure, Townsend's coefficient takes on values of around $10^6\,m^{-1}$, which implies an ionization time of $\tau_{ion} \simeq 10^{-11}\,s$. If a strong electric field is generated, then the main reaction that causes plasma decay is dissociative attachment, whose significant time scales are $\tau_{dec} = 10^{-7} - 10^{-8}\,s$. On the other hand, if the electric field is weak and the electron temperature is around $900\,K$, then the main cause of decay is the three-body attachment reaction with its related time of $\tau_{dec} = 10^{-8} - 10^{-9}\,s$.

This vast separation of temporal scales between the different phenomena (from 10^{-12} to $10^{-7}\,s$) generates stiffness in the system of equations previously defined in Chapter 2.5. In order to solve the smallest time scales with an explicit integration scheme, a time step of the order of at least picoseconds ($10^{-12}\,s$) is needed. This means that to simulate flow control for a few milliseconds, it would be necessary to solve the DBD system of equations a billion times, leading to an obviously too computationally expensive simulation. Fully implicit schemes would be the ideal choice to solve a stiff system obtaining stable solutions with an important reduction in time needed. However, due to the coupling between the time-dependent equations for particles and the pure elliptic Poisson equation, this option cannot be implemented without further complicating the model, i.e. without having to solve Maxwell's equations. It is, however, possible to turn the difference of time scales into an advantage by decoupling the four processes described by said scales: drift-diffusion of charged particles, ionization, plasma decay, and relaxation of the electric field. This is a hybrid solution strategy, each subproblem is treated with a so-called calibrated numerical technique (Runge-Kutta or implicit) in order to recover the general stiffness given by the simultaneous resolution of the four problems. This means that a unique integration time step is employed for all of the subproblems. Asynchronous schemes also exist, in which different time steps are used for the different phenomena; an example is presented in Ref. [4].

In order to properly capture plasma formation, refined grids are necessary; the chosen discretization step is equal to:

$$\Delta x = min\left(\alpha^{-1}, \lambda_D\right) \tag{3.5}$$

3.1 Poisson equation

The Poisson equation for electric potential Φ, which represents the electrostatic part of the model, as was discussed in the previous chapter, can be decoupled from the plasma evolution problem. The Poisson equation is relaxed considering frozen particles density, while the continuity equations are solved under a frozen electric field.

It is fundamental to properly capture the electric field distribution in the bulk because, due to the LFA, all transport and chemical properties depend solely on the local electric field. Also, this strong dependence between charged particles density and electric field defines dielectric relaxation times much smaller than the other mentioned time scales. Therefore, an implicit approach is necessary despite Poisson's equation being elliptic, in order to avoid limitations on the maximum Δt. The method implemented in this thesis is the one defined by Punset, Boeuf et al. in Ref [50], where the Poisson equation was rewritten as:

$$\epsilon_0 \nabla \cdot \epsilon_r \nabla \Phi = -\rho_c^{k+1} = -\rho_c^k - \left(\frac{\partial \rho_c}{\partial t} \right)^k \Delta t = -\rho_c^k + q_e \Delta t \nabla \cdot (\Gamma_+ - \Gamma_- - \Gamma_e)^k \quad (3.6)$$

Substituting the fluxes into the equation, where N_i represents the number of charged species, we obtain:

$$\epsilon_0 \nabla \cdot \left[\epsilon_r + q_e \Delta t \sum_i^{N_i} \mu_i n_i \right] \nabla \Phi^{k+1} = -\rho_c^k + \Delta t \nabla \cdot \left(-\sum_i^{N_i} q_i D_i \nabla n_i + q_e D_e n_e \frac{\nabla T_e}{T_e} \right)^k \quad (3.7)$$

An estimate value of the right-hand side of equation 3.6 at the time step $k+1$ is computed from the equation for charge density:

$$\frac{\partial \rho_c}{\partial t} + q_e \nabla \cdot (\Gamma_+ - \Gamma_- - \Gamma_e) = 0 \quad (3.8)$$

A fully implicit solver based on finite volume discretization (similar to that in Ref. [51]) is then used to relax the Poisson equation until it converges. Fluxes are evaluated through a set of secondary cells built on top of the main grid, where each vertex of the secondary cell sits on the midway point of the side of one of the main cells, as can be seen in the following picture. The values at secondary cell surfaces are calculated through a weighted average of the neighboring values. This method is second-order accurate in space. The Jacobian matrix is evaluated numerically by perturbing, one by one, the cells of the grid and computing the resultant perturbed flux. Finally, the system is solved using a GMRES (Generalized Minimal Residual Method) iterative method with an incomplete LU factorization. The use of preconditioning techniques is common when handling multiple scale

problems. The solutions obtained with this method were proved to be stable and accurate enough for integration steps up to 50 times larger than the dielectric relaxation time [50].

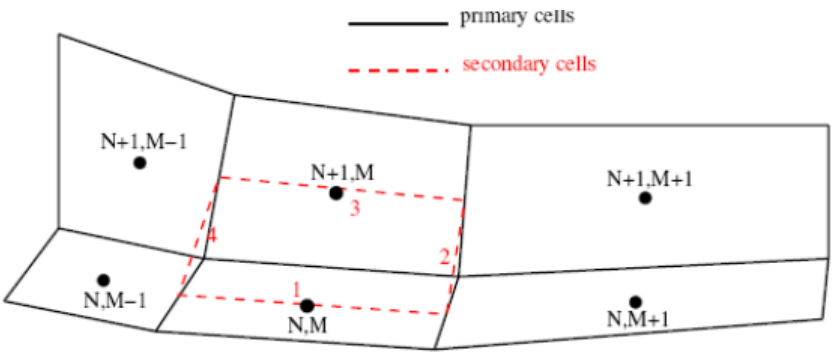

Figure 3.1: Secondary cells

3.2 Continuity equations for charged particles

The main issue in solving the continuity equations for charged particles, in their drift-diffusion approximation, are the very fast chemical rates, specifically decay rates, which cause the source terms to be unstable in the bulk. The Strang splitting method [52, 53] is used as a solver; this is a fractional step integration approach which treats drift-diffusion terms and source terms individually by separating the problem into two sub-problems: a pure advection-diffusion one and a chemical one. This method derives from the more general Godunov splitting approach, but unlike it, this one is second order accurate. Fractional-step methods have the main advantage of being able to use standard schemes for each of the subproblems [53]. The homogeneous system of continuity equations is, at first, integrated in a time step equal to $\Delta t/2$:

$$\frac{\partial n_i}{\partial t} + \nabla \cdot \Gamma_i = 0 \qquad i = +, -, e \tag{3.9}$$

Then, the solution obtained with this first step is used to integrate the chemical system of ODEs defined by the source terms in the time interval Δt:

$$\frac{dn_i}{dt} = \Omega^i_{ch} \tag{3.10}$$

Finally, the first system (3.9) is integrated again in a half-time step. For both the first and last steps, a finite volume scheme is used to discretize the continuity

equations; they are solved with a fully implicit method, which can be either a backward Euler or a trapezoidal scheme, in order to safely manage the coupling between drift (advective) and diffusive terms [54]. An advantage of using a fractional-step approach is that even for implicit schemes, the equations obtained in the i-th cell are decoupled from the equations of all other cells and, therefore, are relatively easy to solve [53].

To implement charged particle fluxes, a Scharfetter-Gummel approach is implemented [55, 56], which provides accurate and stable solutions, especially when an exponential growth of charged particles is present in the bulk, much like in discharge plasmas due to the avalanche ionization. Considering two neighboring cells, i and $i+1$, divided by the interface $i+\frac{1}{2}$, as in Fig. 3.2, the flux through the wall can be expressed as:

$$\Gamma_s^{i+\frac{1}{2}} = \nu_x \frac{n_s^i - n_s^{i+1} e^{-\lambda_x}}{1 - e^{-\lambda_x}} \tag{3.11}$$

where s represents the s-th species and

$$\lambda_x = \pm \frac{\mu_s \mathbf{E} \cdot \mathbf{n}^{i+\frac{1}{2}} \Delta x}{D_s} \tag{3.12}$$

$$\nu_x = \pm \mu_s \mathbf{E} \cdot \mathbf{n}^{i+\frac{1}{2}} \tag{3.13}$$

with $\mathbf{n}^{i+\frac{1}{2}}$ being the normal to the interface. As for the Poisson equation, Jacobians are calculated numerically, only once for a global Strang step. This can be done thanks to the linear nature of the homogeneous system of continuity equations with respect to particle number densities.

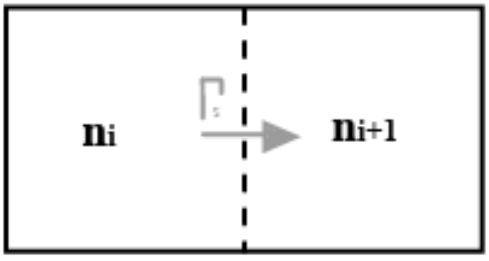

Figure 3.2: Flux at the interface of two neighboring cells

Inevitably, the use of a fractional step method like this one introduces an error with respect to a non-split scheme; in this particular case the error is of the order of Δt^3 and the solution is, at best, second order accurate, given that every step has an accuracy of at least second order.

3.3 Source terms

In order to obtain source terms, a standard explicit Runge-Kutta method, accurate to the second order is typically able to capture stable solutions [40]. However, due to the presence of different time scales between ionizing and plasma decay terms, some stiffness could arise. Considering the non-linear ODE for electrons, neglecting every process except three-body attachment for simplicity:

$$\frac{\partial n_e}{\partial t} = \alpha \mu_e n_e ||\mathbf{E}|| - \nu_{att} n_e \tag{3.14}$$

Depending on the local electric field, this equation describes either an exponential growth (due to primary avalanche ionization) or an exponential decay (due to attachment) of electron number density, with a characteristic frequency of:

$$\nu = \alpha \mu_e ||\mathbf{E}|| - \nu_{att} \tag{3.15}$$

which is large and either positive or negative depending on which process dominates on the other. To correctly solve equation 3.14, the needed time step has to be of the order of magnitude of the fastest time scale between the two processes:

$$\Delta t_{ion} = min\left(\frac{1}{\alpha \mu_e ||\mathbf{E}||}, \nu_{att}^{-1}\right) \tag{3.16}$$

which is called the ionization limit. Using a bigger time step introduces instabilities in the solution of the drift-diffusion equations. This happens mainly when decay rates are dominant: plasma decays so quickly that explicit integrations with steps larger than the ionization limit produce numerical oscillations that blow up the solution. Thus, an implicit scheme has to be used in these cases. On the other hand, however, when the ionization rates are dominant (pure ionization process), using explicit integration schemes does not affect the stability whatsoever but it could lead to an over- or under-estimation of electron density influencing the accuracy of the overall solution. Now the time steps are relatively limited by the Maxwell time and solutions become unstable if too large time steps are used, leading to the definition of a new time limit:

$$\Delta t \leq 50 \tau_{rel} = \frac{50 \epsilon_0}{q_e \sum_i^{N_i} \mu_i n_i} \tag{3.17}$$

In order to avoid these issues the ODE system is split further in a production system of equations, where only the production terms are considered, and a loss system, which includes all decay processes. The production system is solved with a

standard explicit Runge-Kutta scheme RK2 [57]:

$$\frac{dn_+}{dt} = \alpha||\Gamma_e|| \tag{3.18}$$

$$\frac{dn_-}{dt} = (\nu_{att} + \nu_{att,d})n_e \tag{3.19}$$

$$\frac{dn_e}{dt} = \alpha||\Gamma_e|| + \nu_{dO_2}n_- \tag{3.20}$$

The loss system is, instead, solved with an implicit trapezoidal method:

$$\frac{dn_+}{dt} = -\beta_{ie}n_+n_e - \beta_{ii}n_+n_- \tag{3.21}$$

$$\frac{dn_-}{dt} = -\beta_{ii}n_+n_- - \nu_{dO_2}n_- \tag{3.22}$$

$$\frac{dn_e}{dt} = -\beta_{ie}n_+n_e - (\nu_{att} + \nu_{att,d})n_e \tag{3.23}$$

The final solution is obtained with another Strang splitting step, with a global time step lower than the latest defined limit (3.17) in order to ensure stability and accuracy. This second Strang procedure is in every other aspect equal to that described in the previous section (3.2).

3.4 Summary of the numerical scheme

To solve the case studies a FORTRAN code was used which works as follows:

1. Definition of the grid and starting values of parameters
2. Solution of the Poisson equation following the scheme described in 3.1
3. Solution of the continuity equations through Strang Splitting:
   (a) Predictor step: solution of the homogeneous system 3.9 using a $\Delta t/2$ time step
   (b) Solution of the chemical system of ODEs (3.10)
   (c) Corrector step: new solution of the homogeneous system with a half-time step using the updated values from the previous step
4. Treatment of the source terms
5. Final solution of the continuity equations for charged particles (like Step 3)
6. Definition of the surface charge density σ and the EHD force $\mathbf{F} = \rho_c\mathbf{E}$

Chapter 4

Results

Here we show the most significant results obtained by implementing the numerical model. All studies were conducted on the classical Single-Dielectric Barrier Discharge configuration. The computational volume considered is two-dimensional as the effect of the actuators is mainly in the direction of the flow and in the direction perpendicular to the wall. This simplifies the problem, however, it has been found that 2D simulations tend to underestimate the extension of the force field and its amplitude because of a weaker electric field concentration in the two-dimensional structures of plasma [31]. In fact, streamers are highly unstable structures, which leads to branching in different directions: this phenomenon is not captured unless a three-dimensional approach is considered [40]. Regardless, to keep the simplicity of the model a 2D approach is believed to be accurate enough for our study. The geometry of the domain is represented here:

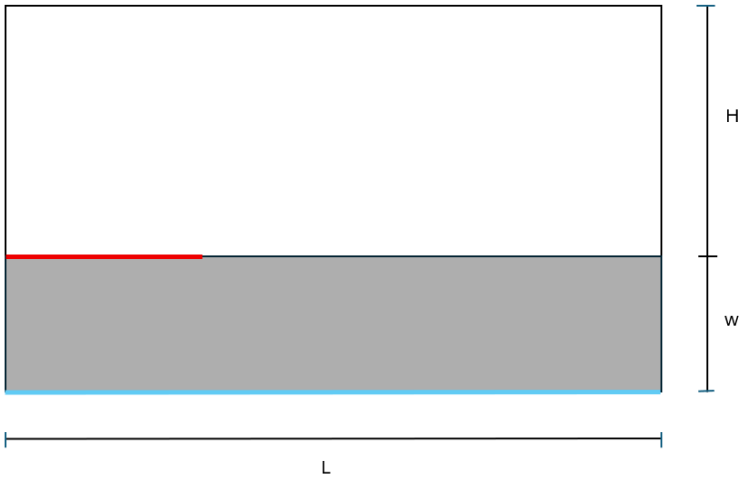

Figure 4.1: Computational domain

The blue line represents the buried electrode, while the red line represents the exposed one, the dielectric is the area in grey. The electrodes are considered infinitely thin since multiple experiments performed with both buried and slightly protruding electrodes have shown no considerable difference in actuator performance [25]. The dimensions of the domain are $H = 0.1\,mm$, $L = 0.4\,mm$ and $w = 0.05\,mm$, and the grid is made up of 200×75 elements, meaning that each cell side is $\Delta x = 2\,\mu m$ long.

The computational grid is divided into two blocks of the same length, one above the other. The first one encloses the air portion of the domain and has external flow on all its sides except the lower one where it touches the exposed electrode first and the dielectric wall second. The second block encompasses the dielectric and meets both electrodes, respectively, on its upper and lower side. The two blocks have the same number of cells in the horizontal direction and they're built in a way that their cells match (the nth cell on the lower side of the first block borders the nth cell on the upper side of the second block). The secondary grid is built as described in Chapter 3.

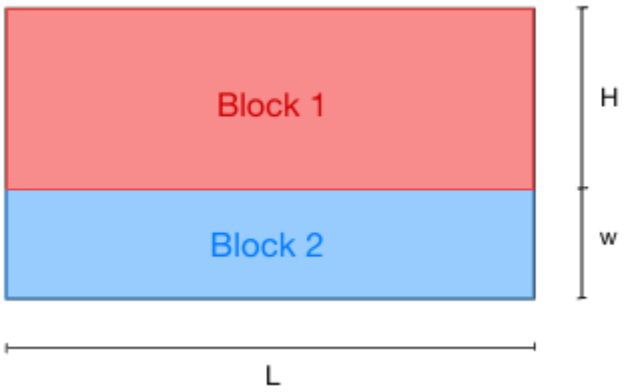

Figure 4.2: Discretization grid

The case studies differ in a number of parameters: power supply, temperature and charge number density, relative dielectric constant, as well as the position of the two electrodes. The goal is to obtain visual representations and numerical values for charge density, electric potential and electrohydrodynamic force for each case in order to see how these parameters evolve during the discharge life. The effect of various input parameters will also be discussed by comparing different cases.

4.1 DC discharges

4.1.1 Case 1: exposed anode

The first case test is powered by a direct current supply with a voltage of $V = 1200\ V$. The anode is the exposed electrode, while the cathode is embedded in the dielectric and grounded. The relative dielectric constant is equal to $\epsilon_r = 10$, while both secondary emission coefficients of the electrode and the dielectric wall are $\gamma = 0.05$. Ion temperature, which is considered constant and equal to that of the gas, is $T_i = 350\ K$, while the electron temperature is set to $T_e = 11560\ K$ and is also considered as constant in this simulation. Both electrons and ions have a starting charge number density of $n_0 = 10^{11}\ m^{-3}$. With regard to the chemistry model, only avalanche ionization and ion-electron recombination reactions are implemented. The atmosphere is composed of an ionized molecular nitrogen N_2 mixture, made up of electrons, positive ions, and neutrals. The time step is 40 ps, for a total simulation period of 75 nanoseconds.

Here, the distribution of the electric potential is presented at 20 ns of run time. The function is normalized with respect to the reference potential $\Phi_0 = 1200\ V$. The highest values are found close to the anode; in this first phase of the discharge, a significant potential drop can be seen moving further away from the exposed electrode.

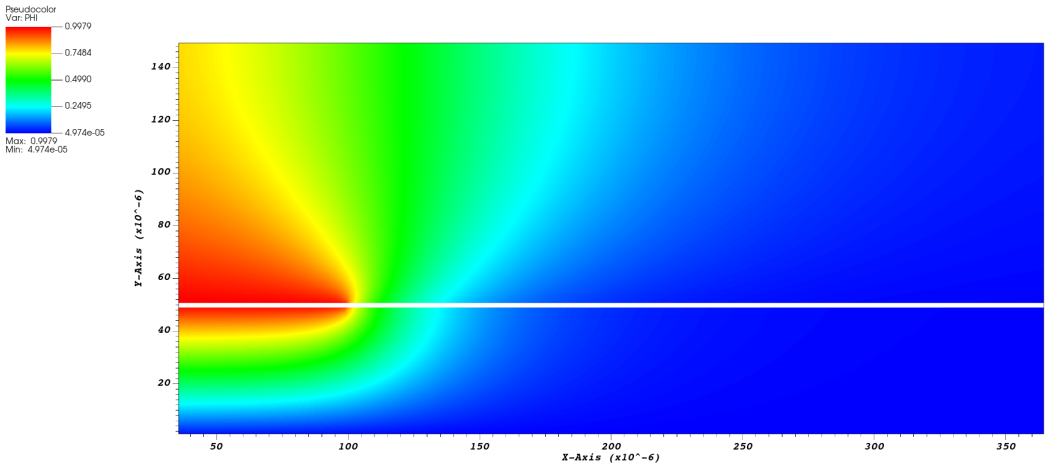

Figure 4.3: Normalized electric potential Φ at 20 ns

Electron and ion charge densities are also shown at the same time step. At the beginning of the discharge, a large collection of ions and electrons forms at the right tip of the anode, right on the surface of the dielectric barrier: this is called a corona regime. At this point, the charge density is not yet high enough to detach from the electrode and is kept anchored where the electric field is the strongest.

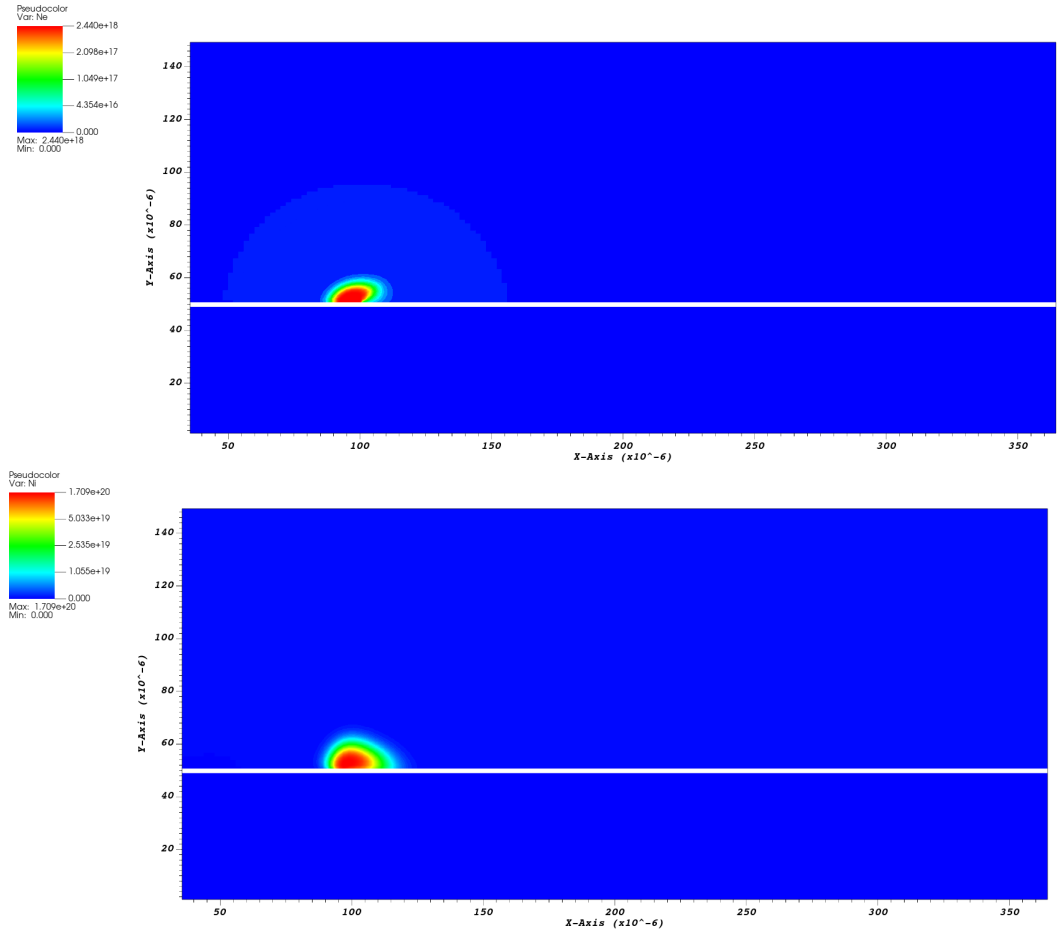

Figure 4.4: Electron n_e and ion n_i densities $[m^{-3}]$ at 20 ns

Once the charge density reaches a threshold, the plasma is able to part away from the anode, and it stars spreading over the dielectric wall due to the difference in electric potential, generating the so-called ionic wind. During this migration, the discharge is kept alive thanks to the secondary emission happening on the barrier surface. As positive ions in movement impact against the dielectric, new seed electrons are produced at the tip of the sheath; these electrons, in turn, trigger new ionization reactions forming more positive ions and electrons, thus sustaining the plasma. At the same time, the ions that deposit on the dielectric charge its surface and reduce the voltage drop between the two electrodes. This causes the plasma sheath to move even further to the right, where the wall is still acting as a cathode, attracting the negative charges. The plasma structure formed by this process is a sheath at the tip of a streamer regime, where the charge density is much lower. The movement of plasma leads, as can be seen, to a wider distribution

of high levels of electric potential.

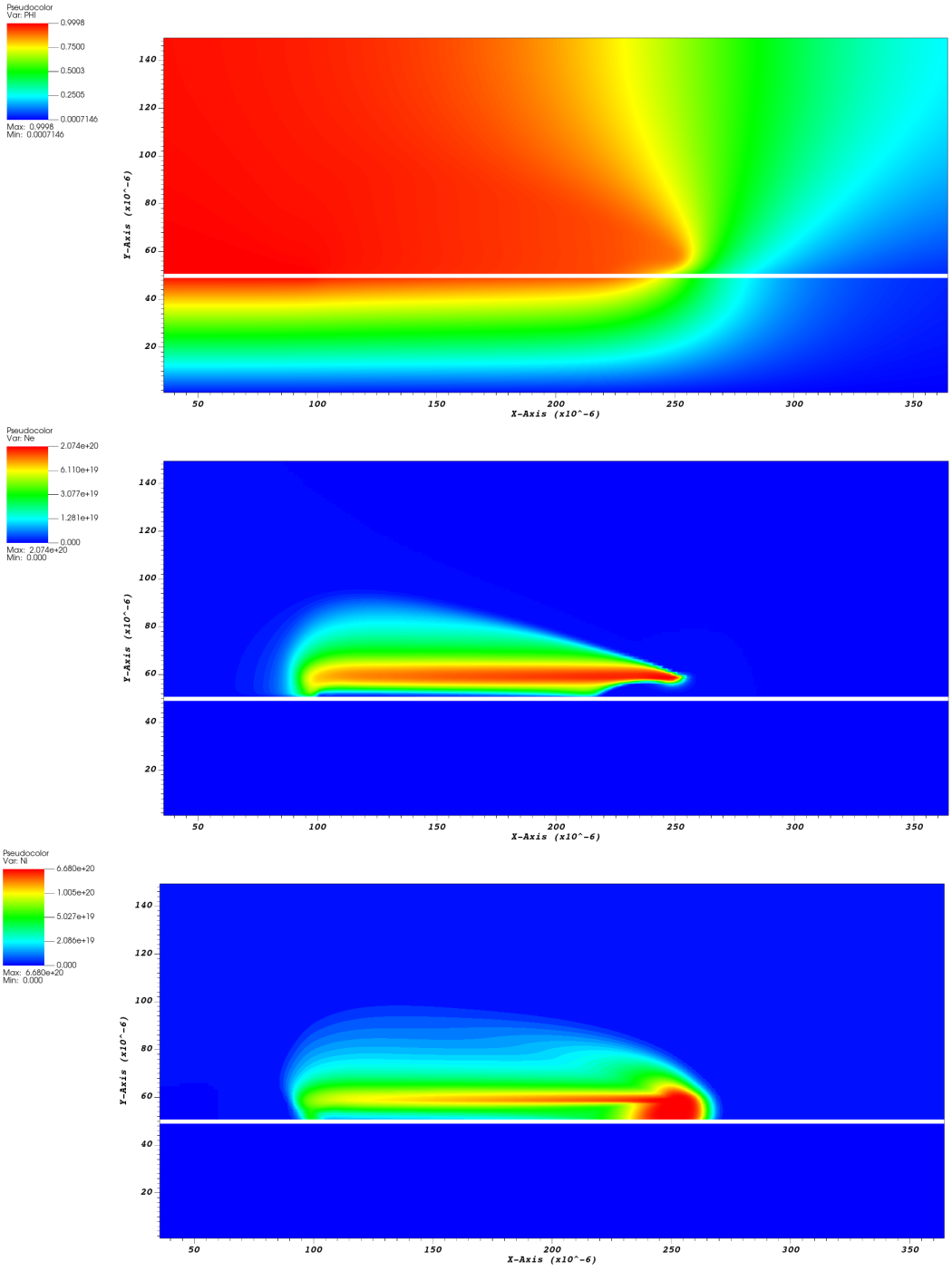

Figure 4.5: Normalized electric potential Φ, electron n_e and ion n_i densities $[m^{-3}]$ at 60 ns

This process only lasts as long as the electric field between the two electrodes is strong enough. Once the sheath is too far from the exposed electrode, the field is too weak and the dielectric does not attract electrons anymore. The plasma sheath stops spreading and disappears quite quickly, because of ion-electron recombination reactions and due to the absence of secondary emission. This self quenching is one of the big advantages of these actuators. As can be seen in the following images, as the plasma moves along the dielectric wall, its charge density in the sheath drops.

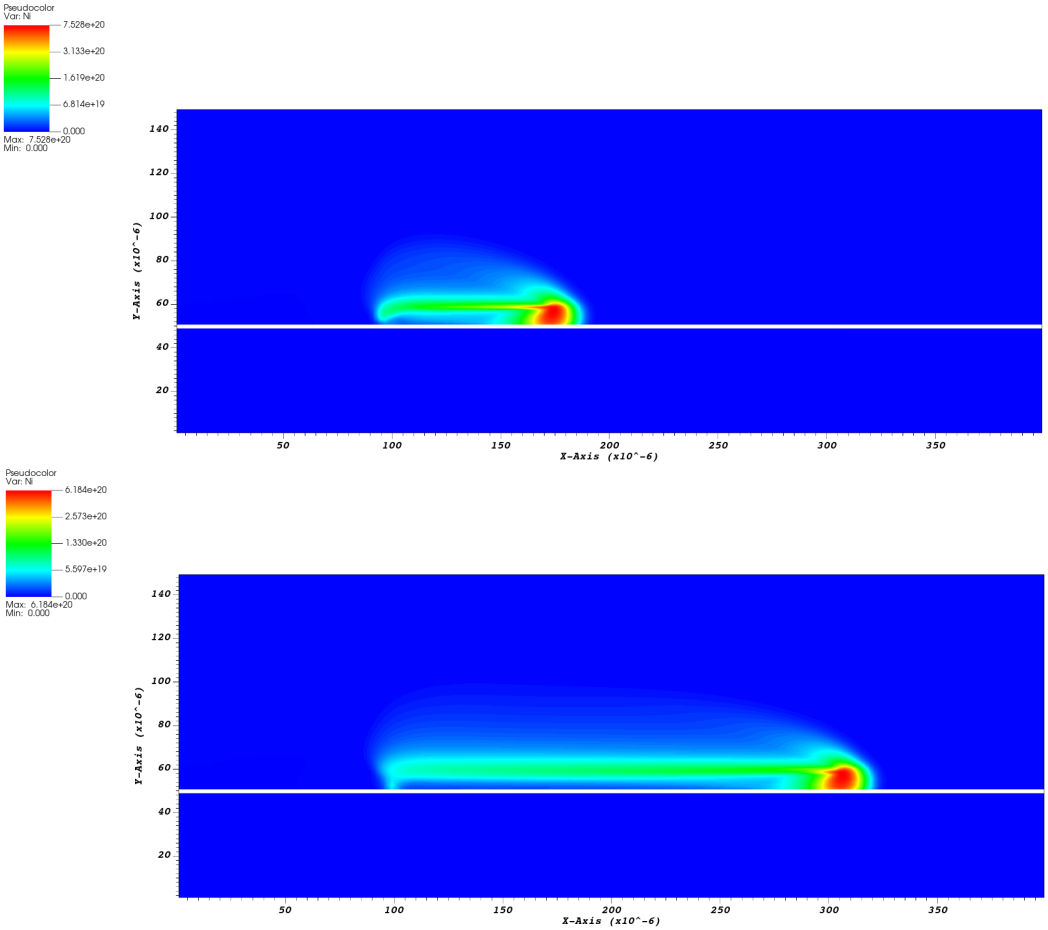

Figure 4.6: Ion density n_i $[m^{-3}]$ at 40 ns and 75 ns

As the ions move along the dielectric they collide against the non-ionized particles, generating a force on the outside flow. This body force is mainly directed towards the dielectric and along the direction of the flow, pushing the neutrals towards the wall and in the streamwise direction, thus delaying flow separation by suppressing contrary gradients. The body force reaches its maximum values near the sheath, where the majority of the ions (which generate the force) are located, while it's

weaker along the streamer. Just like for the charge number density, the intensity of the force shrinks as the plasma moves further from the tip of the exposed electrode. The magnitude of the force vectors starts from $3 \cdot 10^{-3}\ N/m^3$ at 20 ns and reaches values around $12 - 14 \cdot 10^{-3}\ N/m^3$ at its peak before decreasing after the 40-50 ns mark.

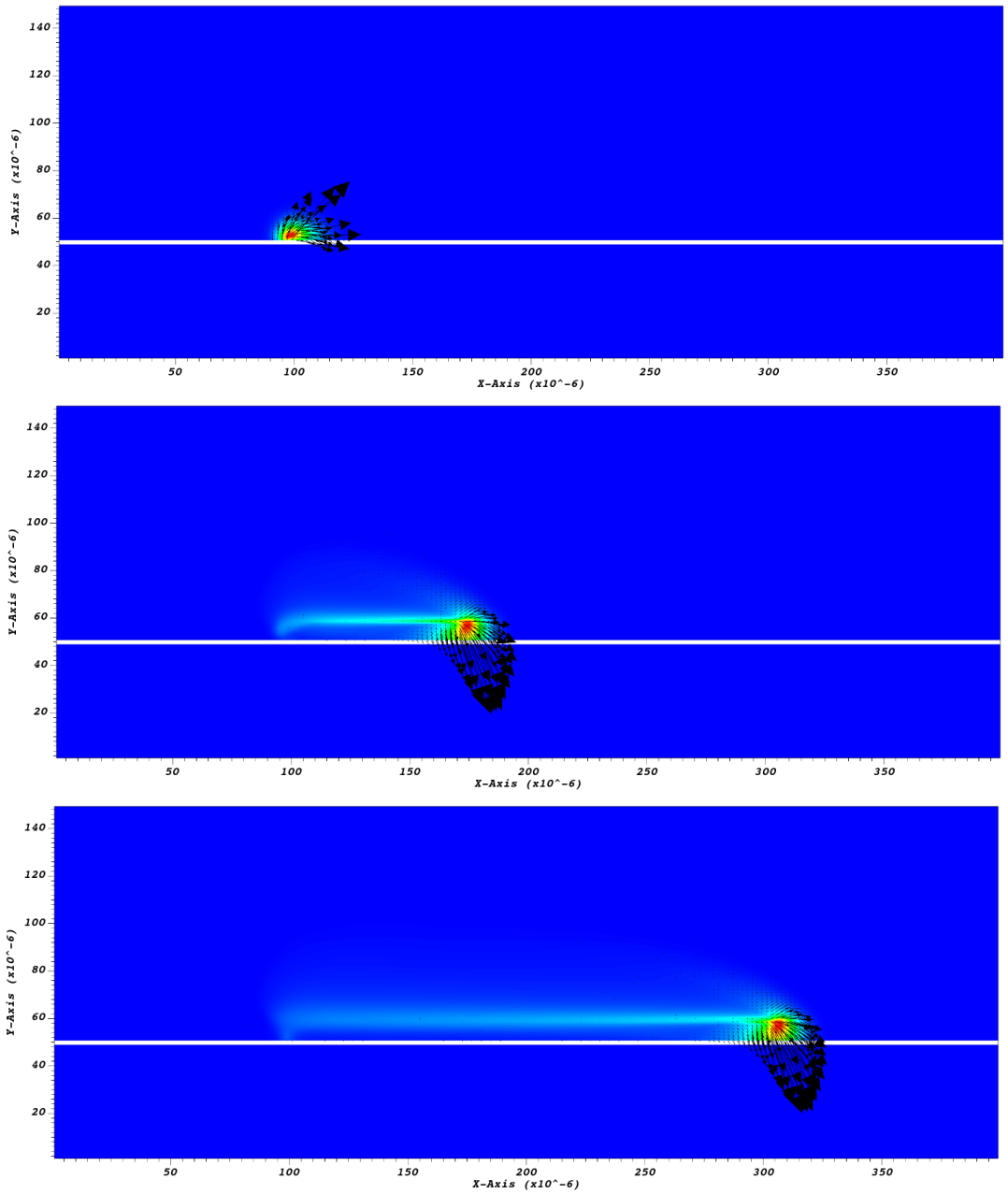

Figure 4.7: Body force **F** vectors at 20 ns, 40 ns and 75 ns

4.1.2 Case 2: exposed cathode

This case study has the same parameters as the previous one:

T_e	11560 K
T_i	350 K
n_0	10^{11} m^{-3}
ϵ_r	10
γ	0.05

Table 4.1: Simulation 2 parameters

It also considers a DC supply, with a reference potential of $\Phi_0 = 1200\,V$ and a nitrogen only atmosphere. The total simulation time is 20 ns with a time step of 5 ps. The main difference from the previous case is the electrodes: the anode is embedded in the dielectric, while the cathode is exposed but still grounded (0 V). Only avalanche ionization and ion-electron recombination are considered for the chemical model.

In this case, the electric field that develops is similar to the previous one but with an opposite polarity, and the resulting electric potential will have an inverse trend, presenting its lowest values near the exposed electrode.

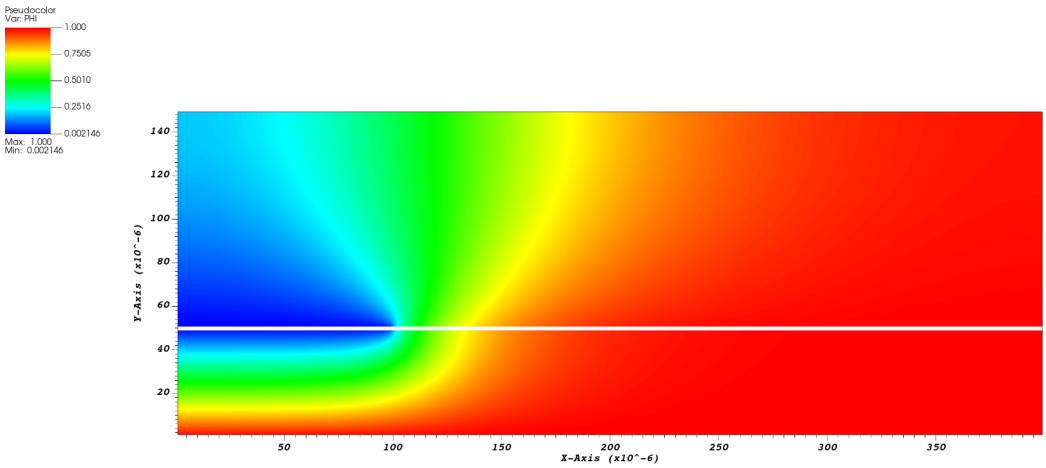

Figure 4.8: Normalized electric potential Φ at 5 ns

Due to a higher ionization rate and more intense secondary emission, discharge develops faster in this simulation, which is the reason for the choice of a smaller time step (one order of magnitude smaller than the previous one).

At first a collection of ions and electrons forms near the tip of the cathode, much like in the previous case, where the electric field is the strongest. Advancing in time, however, a different behaviour can be seen in the plasma. The original sheath remains at the tip of the exposed electrode and does not move, but a filament of plasma (also called a plasma column) starts to spread from the sheath over the dielectric. This is called a corona-like regime. Due to the more intense phenomena mentioned above, higher ion and electron densities are expected with respect to the previous simulation, since the plasma mainly collects in the area of maximum electric field.

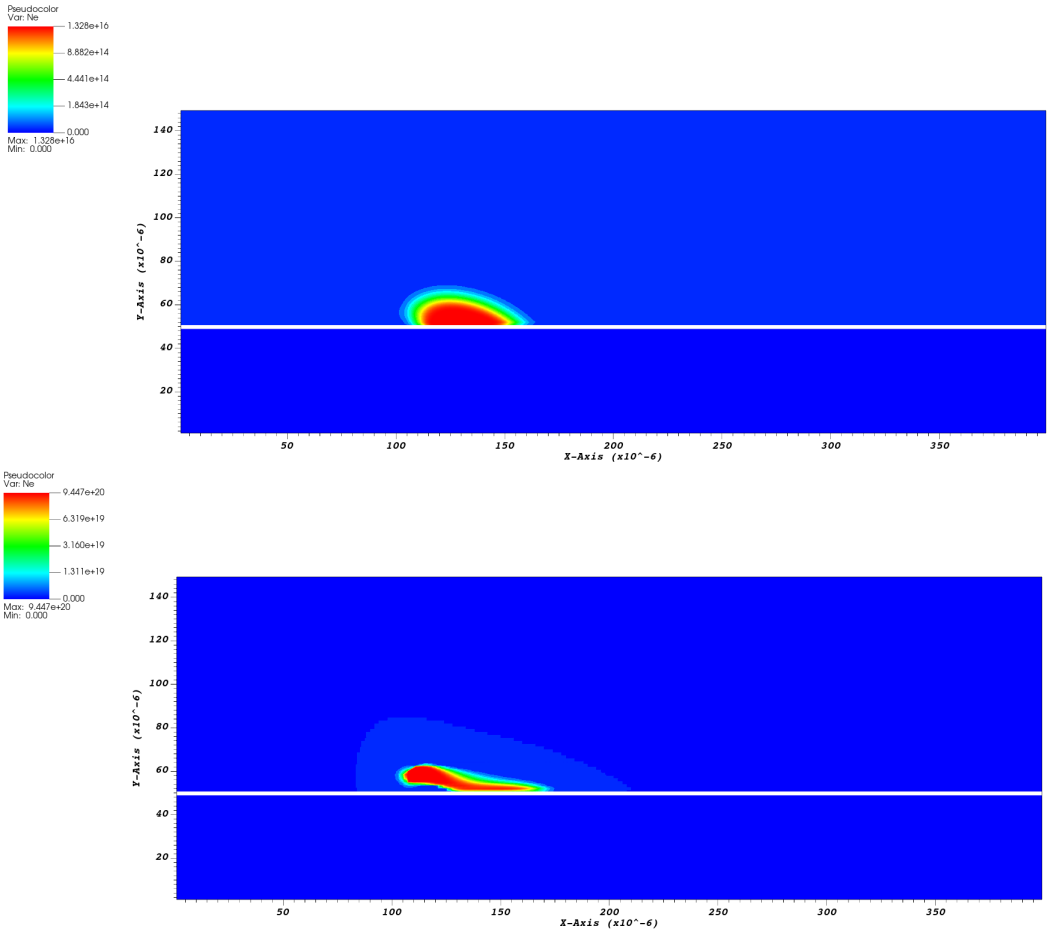

Figure 4.9: Electron density n_e $[m^{-3}]$ at 5 ns and 10 ns

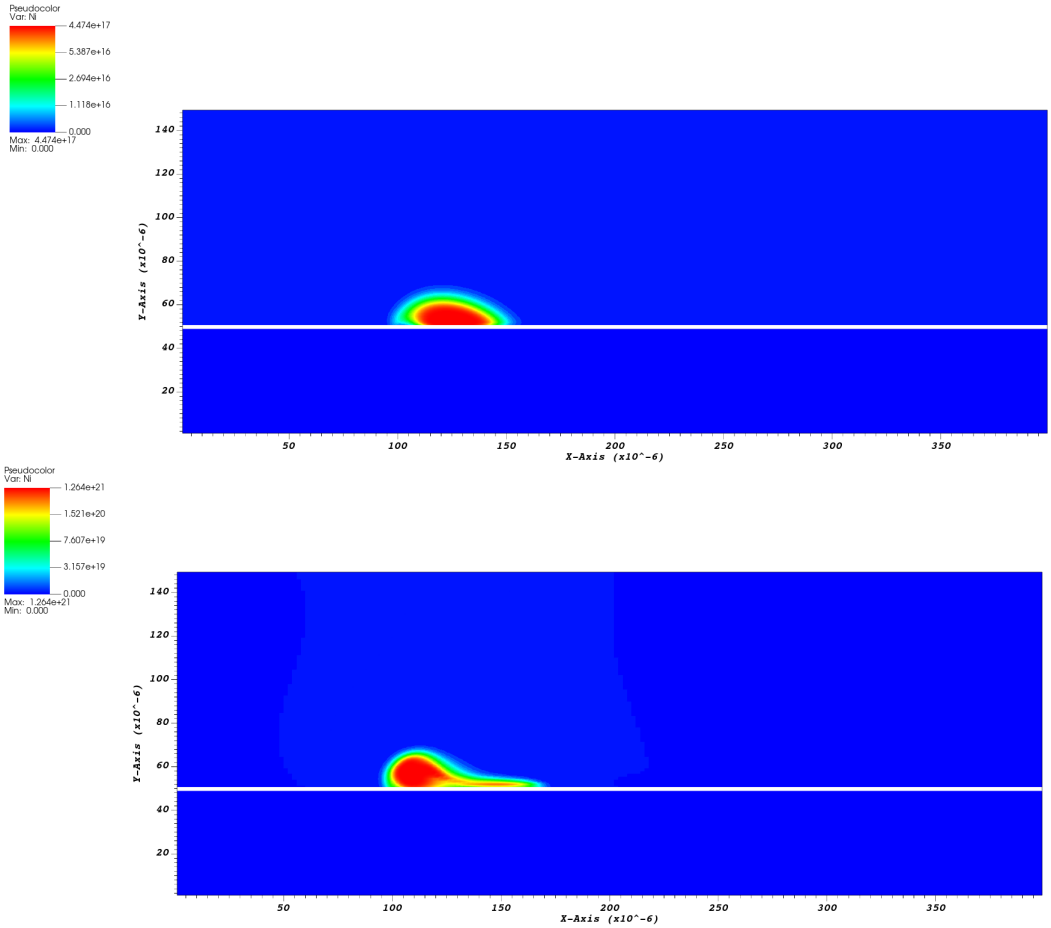

Figure 4.10: Ion density n_i $[m^{-3}]$ at 5 ns and 10 ns

The body force takes on large values near the stationary sheath, while it's negligible everywhere else. At both times (5 ns and 10 ns) the x component of the force is directed in the direction opposite to the flow, but the vertical component switches: at 5 ns it points away from the wall, while at 10 ns it points toward it.

Since in this simulation the region of high concentration is close to the electrode tip i.e. the location with the highest electric field, the force produced will have a higher magnitude than in the previous case with values up to $20 \cdot 10^{-3}$ N/m^3.

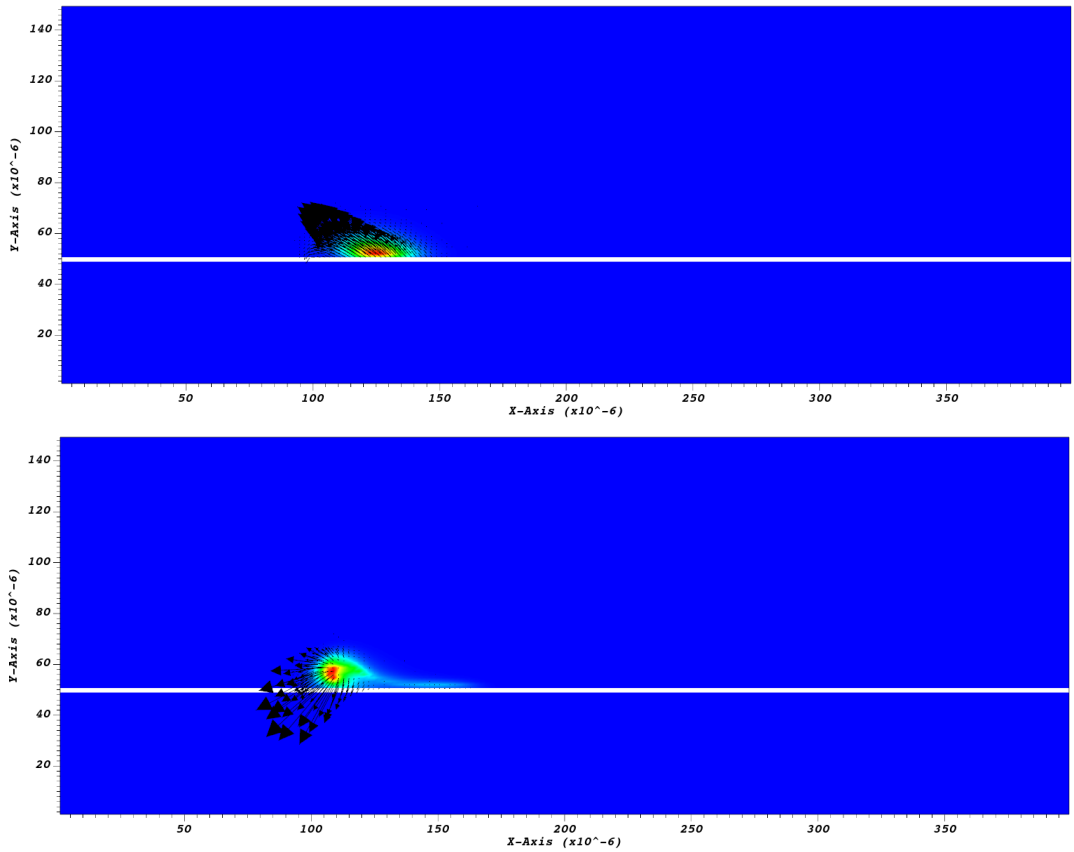

Figure 4.11: Body force **F** vectors at 5 ns and 10 ns

An important element to note is that the processes that take place in a DBD discharge where the exposed electrode is the anode are not perfectly symmetrical to those that take place when the cathode is exposed as one might expect. While the map for electric potential is almost exactly inverted, ion and electron movements are different to the point that two different plasma regimes develop. Also, as can be seen above, the force vectors are not symmetric between the two simulations. This is due to asymmetrical positioning of the two electrodes, which results fundamental when operating the actuator with an AC power supply.

4.1.3 Plasma parameters in time

This simulation is carried out with the same geometry as the first one (exposed anode, grounded and embedded cathode), the input parameters remain the same except for electron temperature and initial charge density. The selected time step is 50 ps and the simulation lasts 100 ns.

T_e	10000 K
T_i	350 K
n_0	10^{13} m^{-3}
ϵ_r	10
γ	0.05

Table 4.2: Simulation 3 parameters

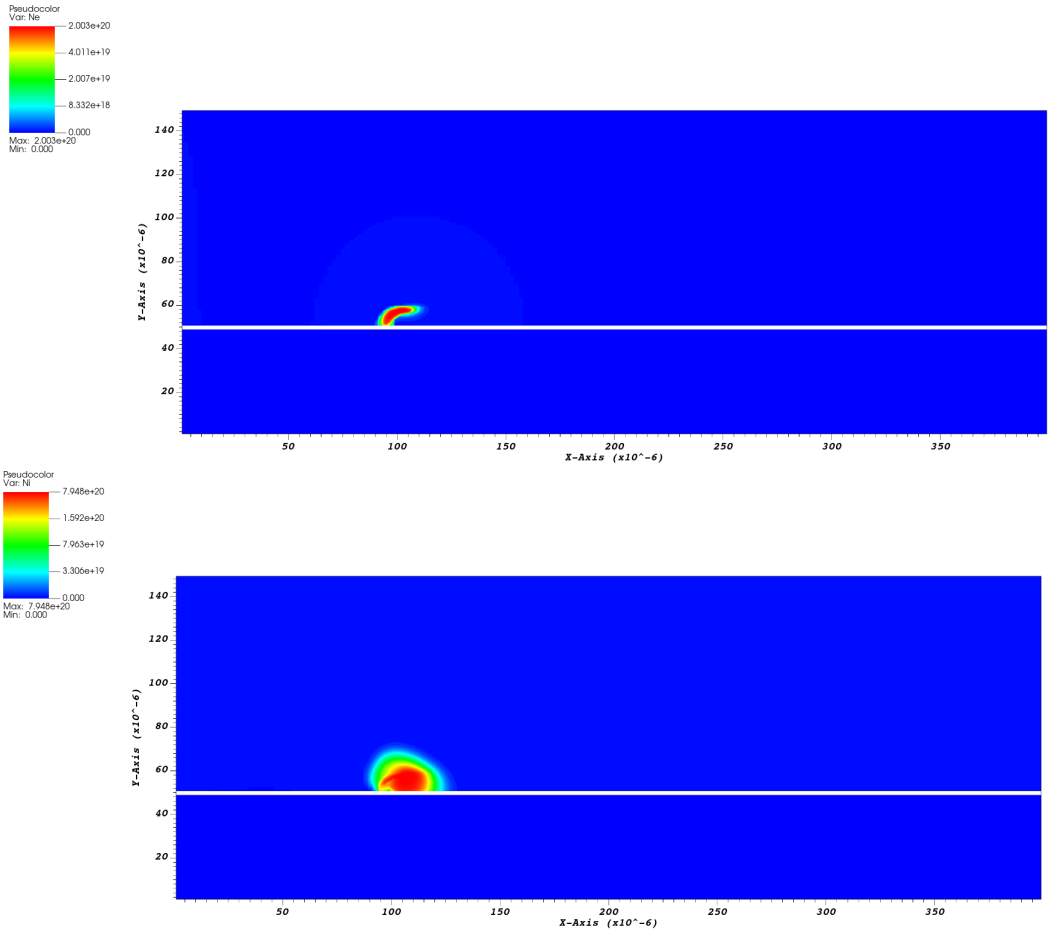

Figure 4.12: Electron n_e and ion n_i densities $[m^{-3}]$ at 20 ns

The results obtained are very similar to those of the first simulation, with a most notable difference in electron and ion number densities in the first time steps due to a higher initial density n_0, while as time progresses this difference reduces.

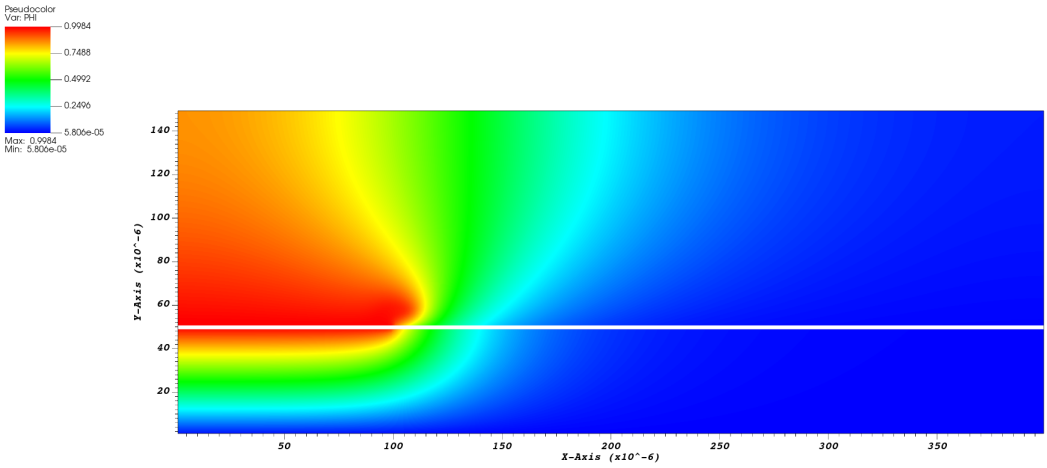

Figure 4.13: Normalized electric potential Φ at 20 ns

Taking into consideration both cases 1 and 3 it is possible to study some trends in how variables change throughout time as the discharge develops, focusing on the density parameters.

Electron density grows initially at a very fast rate due to avalanche ionization: between 20 ns and 40 ns in the first simulation the density becomes four orders of magnitude larger, and in the case n.3 it grows from $10^{13}\ m^{-3}$ to $10^{17}\ m^{-3}$ in the first 10 ns. In the following time steps, this growth rate slows down due to a weaker electric field and the beginning of recombination reactions between electrons and ions. Ion density follows a similar pattern, although its growth rate starts to decline sooner than for electrons due to the dielectric wall "anchoring" positive ions to its surface which diminishes their concentration in the plasma. This phenomenon is more noticeable in the first case. While at the beginning of the simulations ions have a much larger density in the plasma (two-three orders of magnitude larger), as a result of this growth difference, as time goes on the two particle densities get closer and closer. This, in turn, causes a reduction in the charge density $\rho_c = q_e(n_+ - n_e)$, which combined with the reduced electric field, generates a force ($\mathbf{F} = \rho_c \mathbf{E}$) that decreases in intensity as the plasma moves away from the exposed electrode.

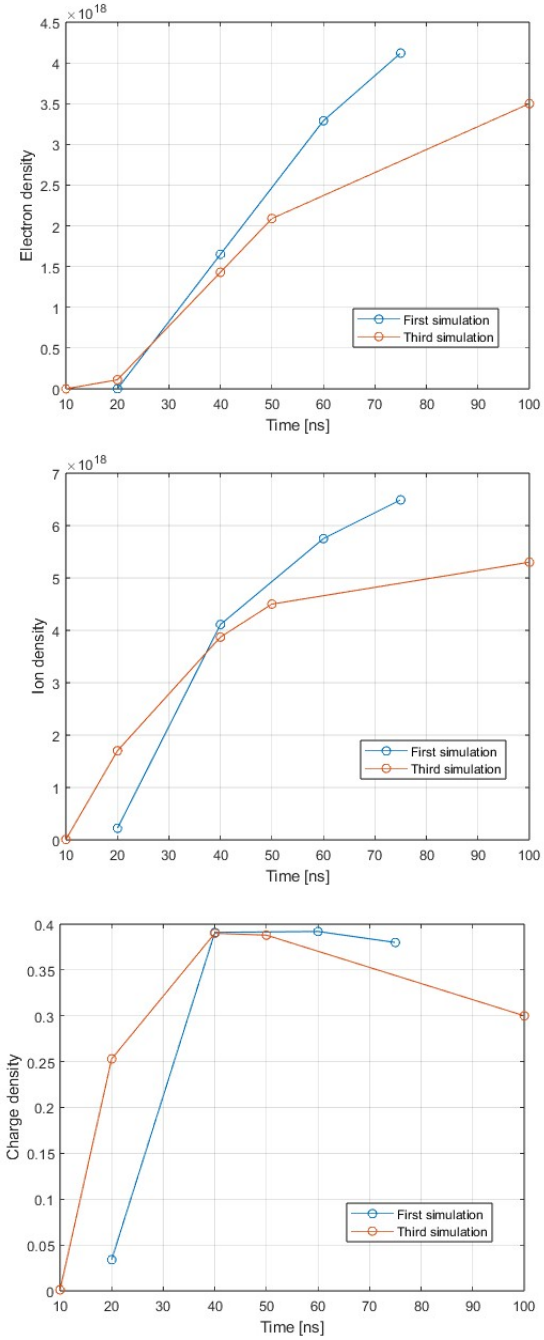

Figure 4.14: Electron density n_e $[m^{-3}]$, ion density n_i $[m^{-3}]$ and total charge density ρ_c $[C/m^3]$ for Cases 1 and 3

The force developed is similar to that of Case 1 (4.1.1), the magnitude is greater near the streamer head and almost negligible along the filament, as the plasma sheath moves away from the anode, its intensity diminishes.

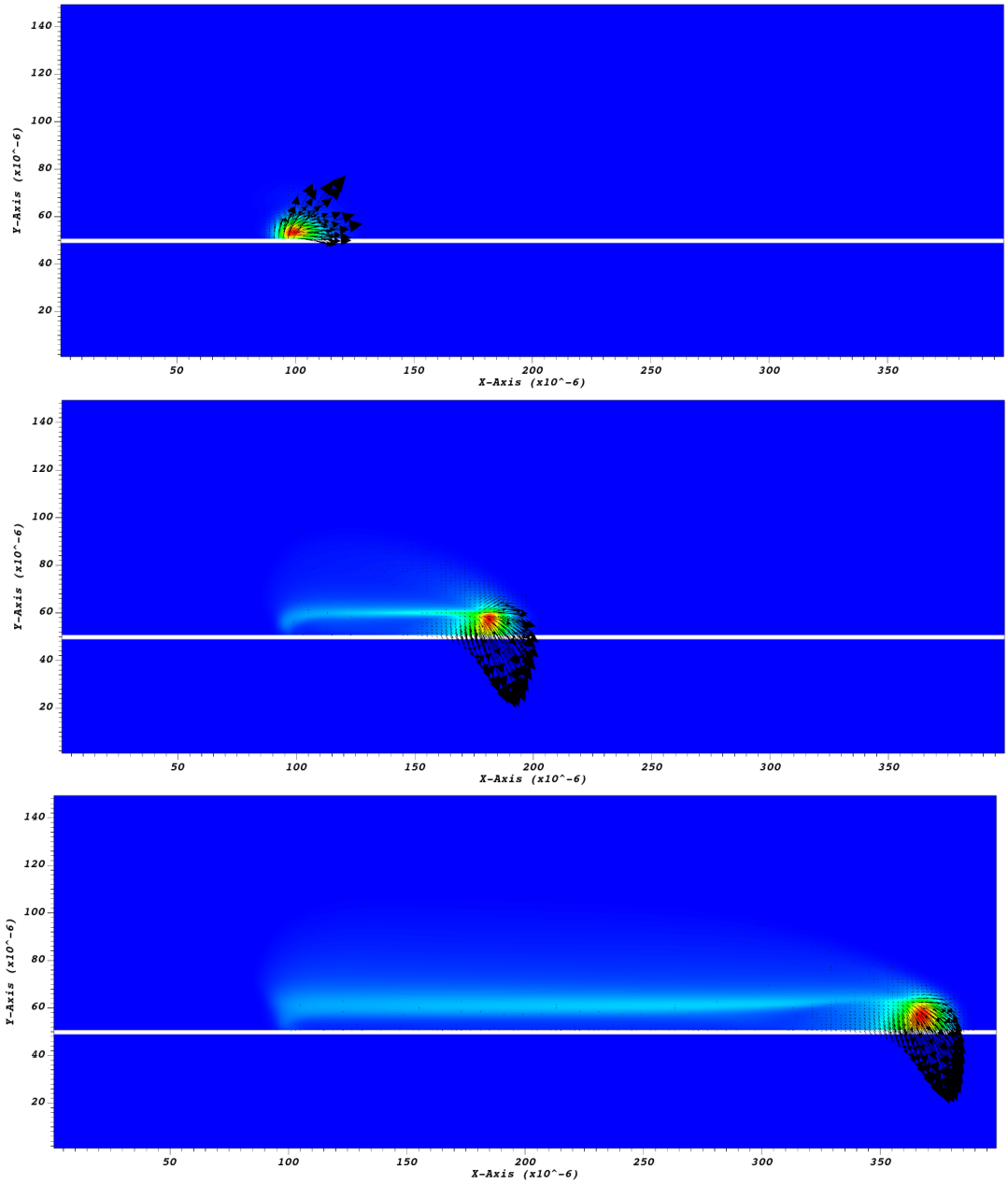

Figure 4.15: Body force **F** vectors at 10 ns, 40 ns and 100 ns

4.1.4 Effect of relative dielectric permittivity

Two more test cases were conducted, with the same input parameters as Case 1, but with different values of relative permittivity in order to study its influence on the discharge. The first case had a permittivity of $\epsilon_r = 5$ and the second of 15, while Case 1 (4.1.1) used a value of 10.

Firstly we compare electron and ion densities of the three simulations at a relatively early time, 20 ns.

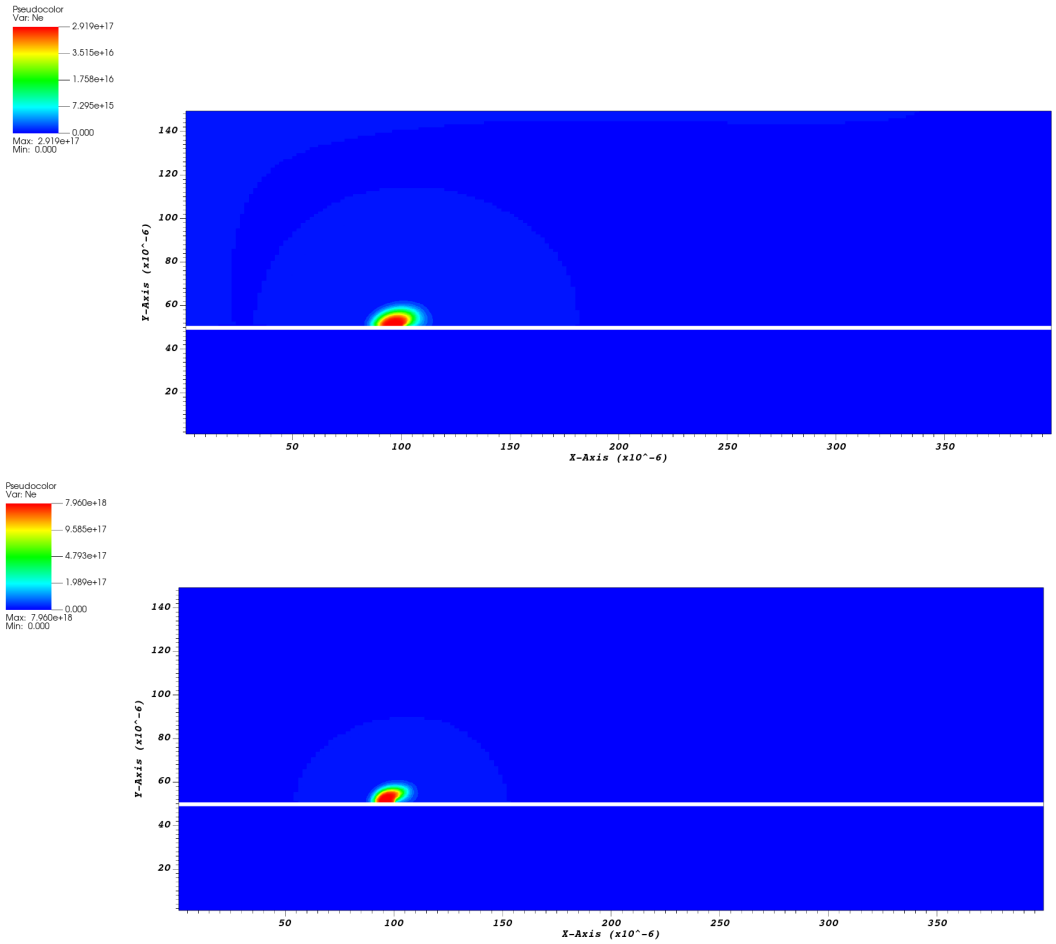

Figure 4.16: Electron densities n_e $[m^{-3}]$ at 20 ns with $\epsilon_r = 5$ (above) and $\epsilon_r = 15$ (below)

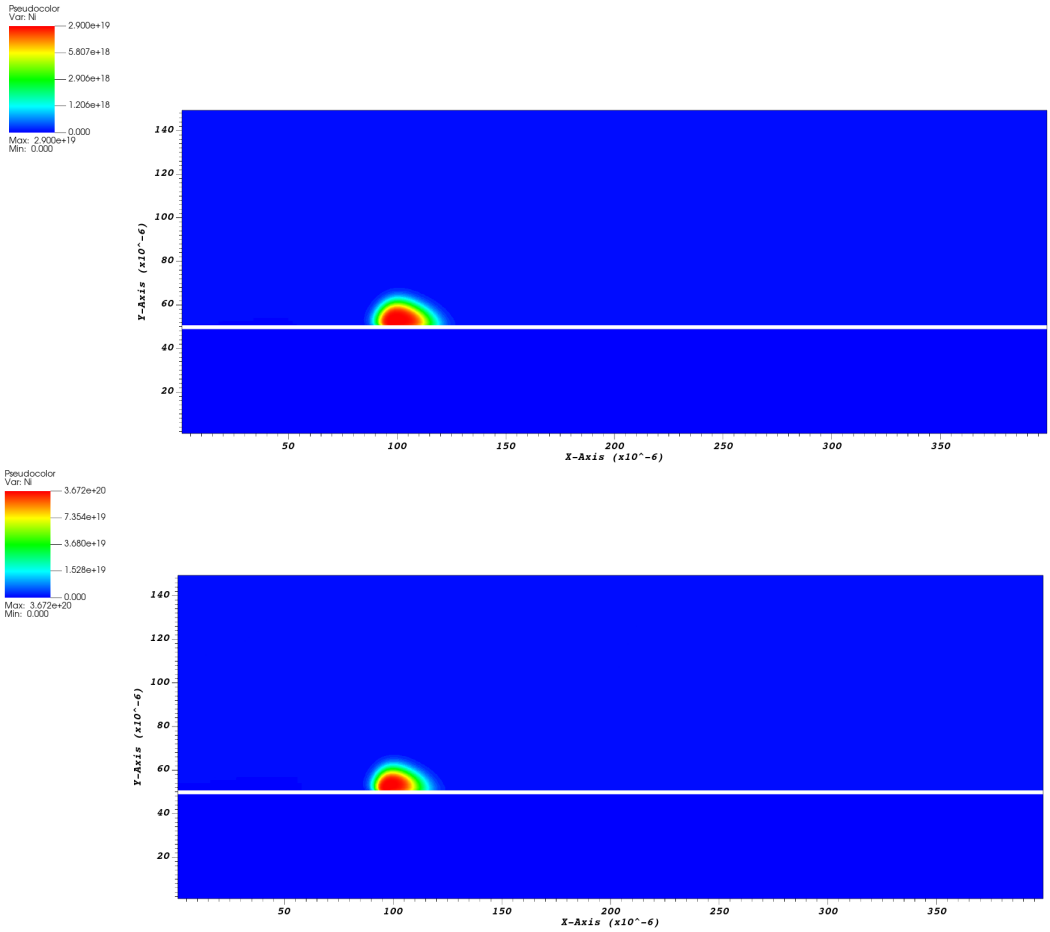

Figure 4.17: Ion densities n_i $[m^{-3}]$ at 20 ns with $\epsilon_r = 5$ (above) and $\epsilon_r = 15$ (below)

A higher relative dielectric permittivity leads to the formation of a stronger electric field and therefore to greater ionization and a higher density of charged particles (both electrons and ions). In the streamer head, where densities are at their greatest, electron density grows from $10^{17}\ m^{-3}$ with $\epsilon_r = 5$ to $10^{18}\ m^{-3}$. Similarly, ion density is one order of magnitude higher in the second case.

The higher electric field and charge density lead to a stronger force imparted on the neutrals, as can be seen in the following images. Maximum values for body force and densities at the three permittivity levels are also presented below.

ϵ_r	$\mathbf{F}_{max}\ [N/m^3]$	$n_{e,max}\ [m^{-3}]$	$n_{i,max}\ [m^{-3}]$
5	$6 \cdot 10^{-4}$	$2.92 \cdot 10^{17}$	$2.9 \cdot 10^{19}$
10	$3 \cdot 10^{-3}$	$2.43 \cdot 10^{18}$	$1.7 \cdot 10^{20}$
15	$6 \cdot 10^{-3}$	$7.96 \cdot 10^{18}$	$3.67 \cdot 10^{20}$

Table 4.3: Evolution of maximum values with relative permittivity

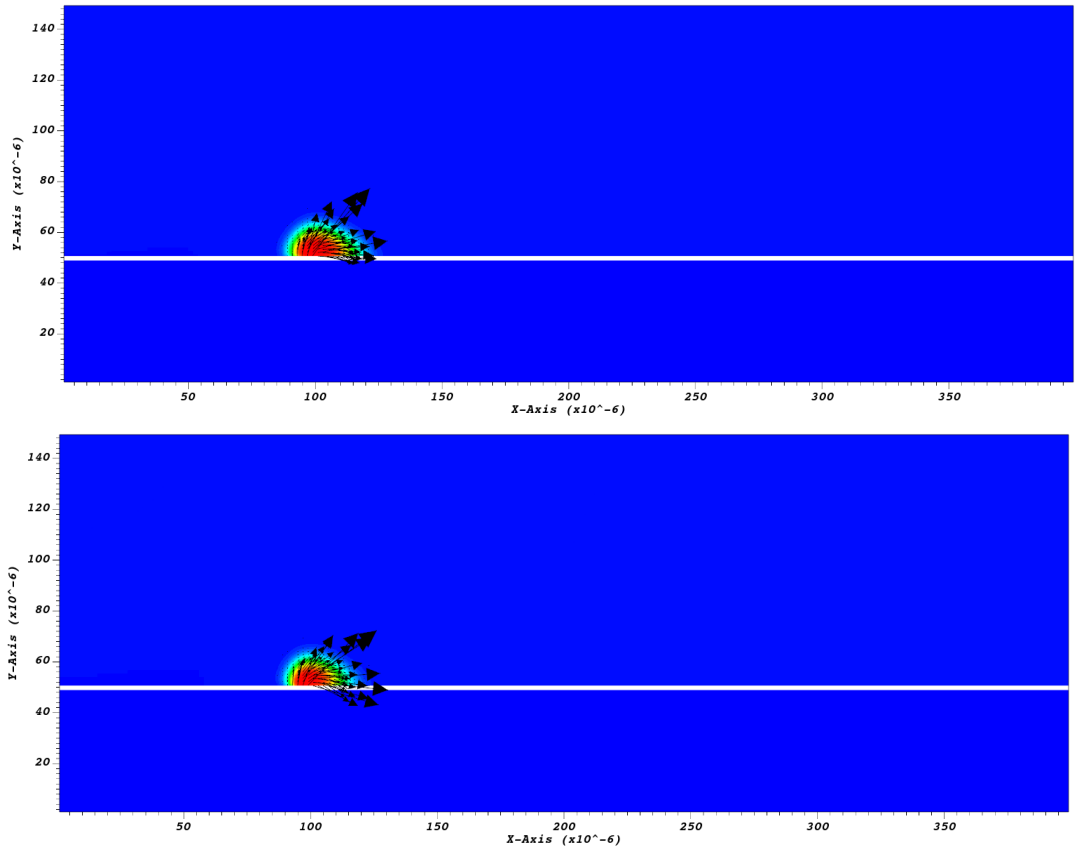

Figure 4.18: Body force **F** vectors at 20 ns with $\epsilon_r = 5$ (above) and $\epsilon_r = 15$ (below)

Now we compare the same quantities but at a later time stamp: 60 ns. At this point, the discharge is completely developed and recombination processes are starting to become more relevant. As can be seen in the image below (4.19), in the case of a higher dielectric permittivity, the ionic wind is faster, meaning that in these 60 ns the plasma has spread further from its origin, the tip of the exposed electrode. This means that now the streamer head is in a location with a lower electric field than when $\epsilon_r = 5$, ionization reactions are weaker and recombination begins to dominate. In fact, comparing electron and ion densities for the three permittivity values it can be seen that from $\epsilon_r = 5$ to 10 densities grow, while from $\epsilon_r = 10 - 15$ ion density grows very little and electron density even diminishes.

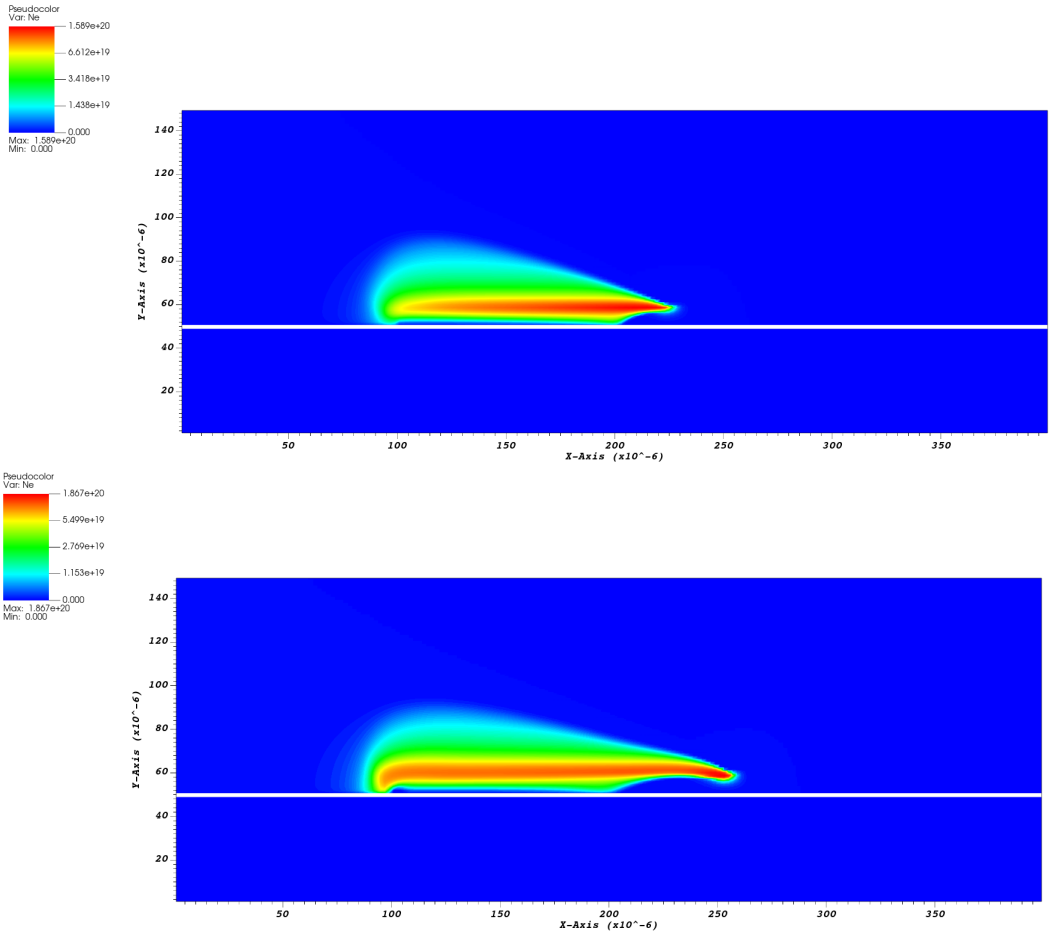

Figure 4.19: Electron densities n_e $[m^{-3}]$ at 60 ns with $\epsilon_r = 5$ (above) and $\epsilon_r = 15$ (below)

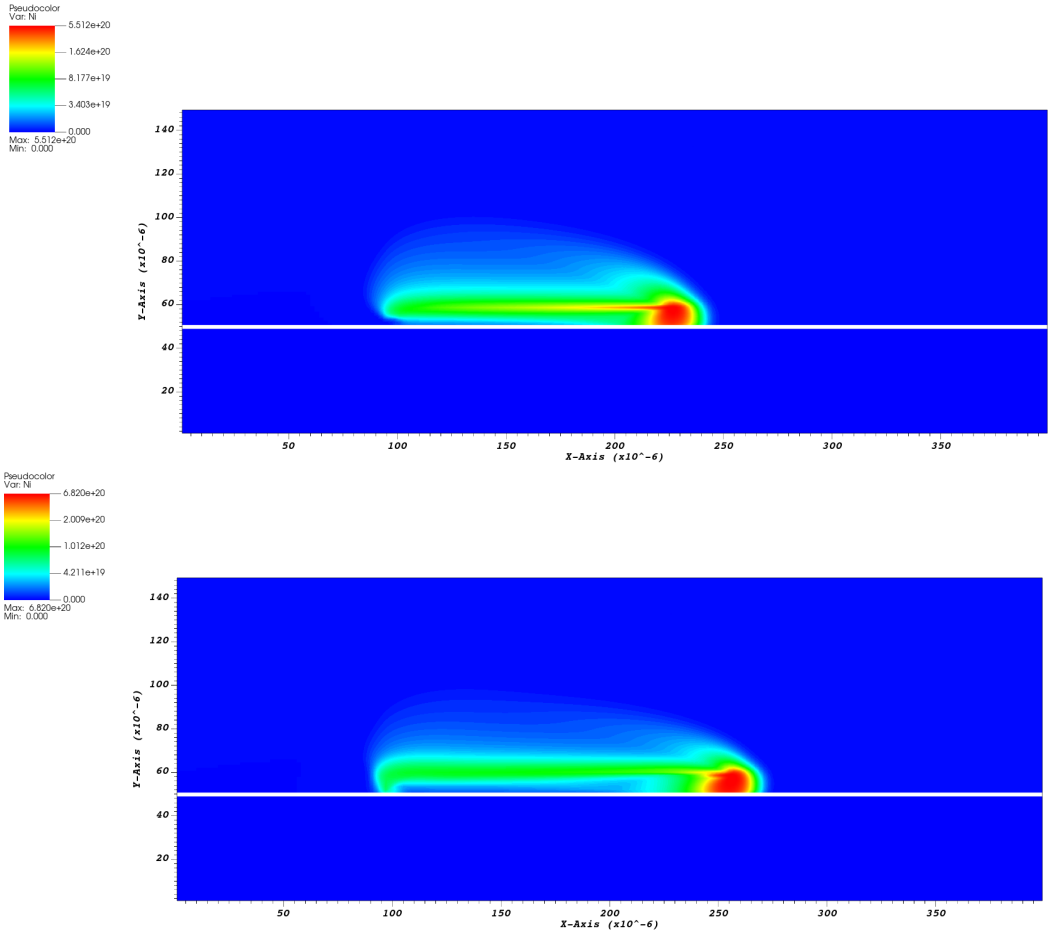

Figure 4.20: Ion densities n_i $[m^{-3}]$ at 60 ns with $\epsilon_r = 5$ (above) and $\epsilon_r = 15$ (below)

This leads to a slower growth rate for the body force: it almost doubles between the first two cases, while its maximum value for $\epsilon_r = 15$ is less than 10% larger than for $\epsilon_r = 10$. If we were to analyze a later time, we would probably see a decline in both densities and in the force as well

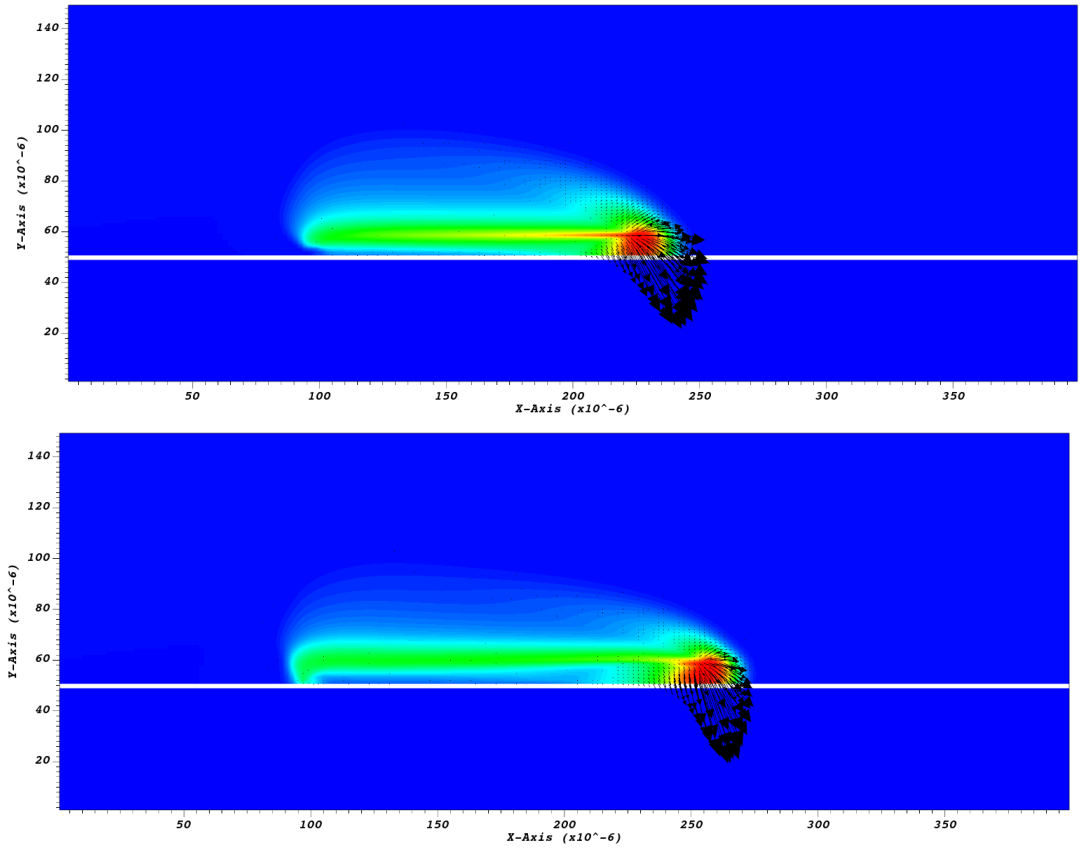

Figure 4.21: Body force **F** vectors at 60 ns with $\epsilon_r = 5$ (above) and $\epsilon_r = 15$ (below)

4.1.5 Effect of voltage

The last study considers the effect of voltage amplitude on the discharge. A test similar to Case 1 except for the supply voltage, 2000 V is conducted. in order to compare the results between the two.

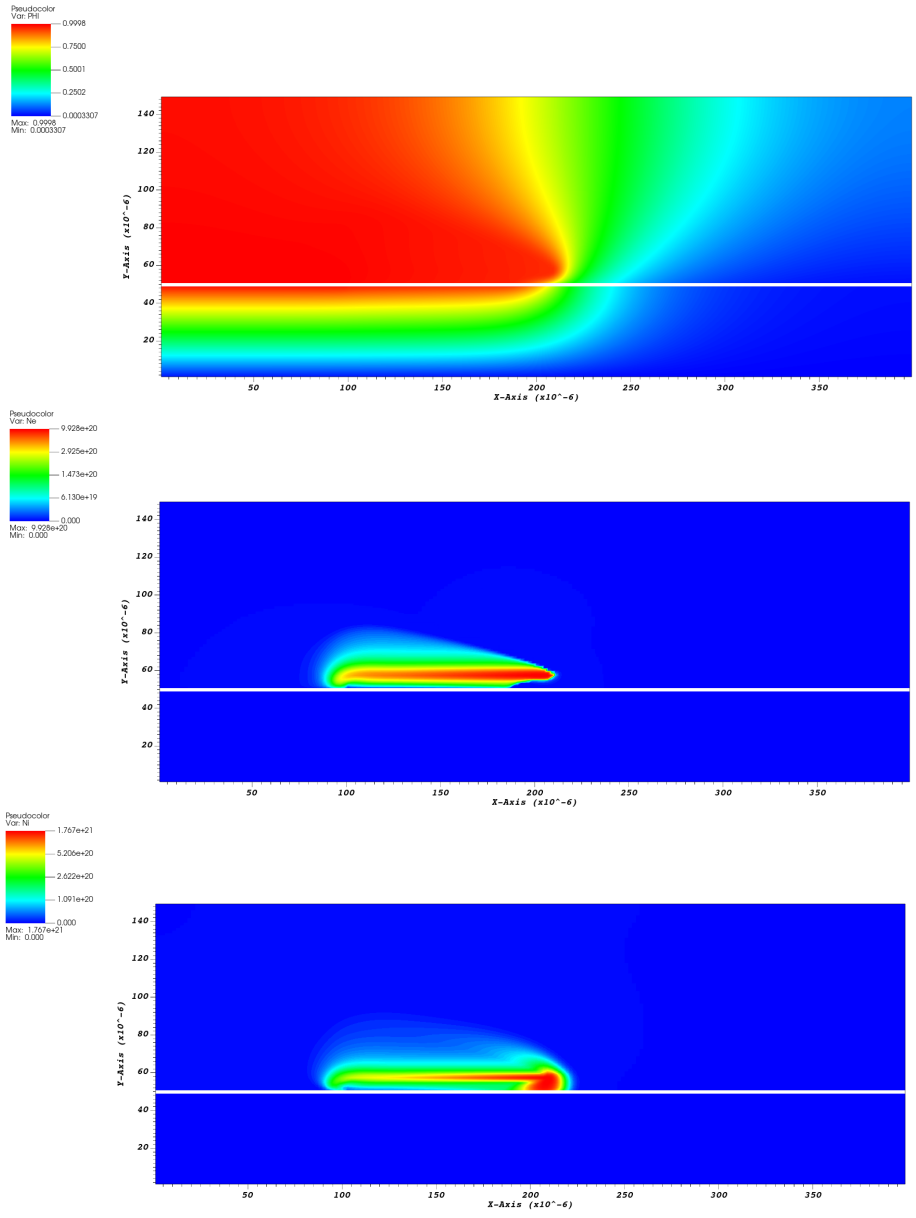

Figure 4.22: Normalized electric potential Φ, electron n_e and ion n_i densities $[m^{-3}]$ at 20 ns

A higher input voltage results in a stronger electric field, and therefore higher number densities and a stronger body force. It also generates a faster ionic wind, meaning that the plasma discharge spreads faster over the dielectric, leading to a reduction in operating time. Since the discharge develops more quickly, it is necessary to compare the two case studies ($1kV$ and $2kV$) at low time steps, to prevent the higher-voltage discharge from dissipating. In fact, at the 40 ns mark in the $2kV$ case the discharge has already reached its maximum expansion, while in the $1kV$ case it's merely halfway through the grounded electrode width.

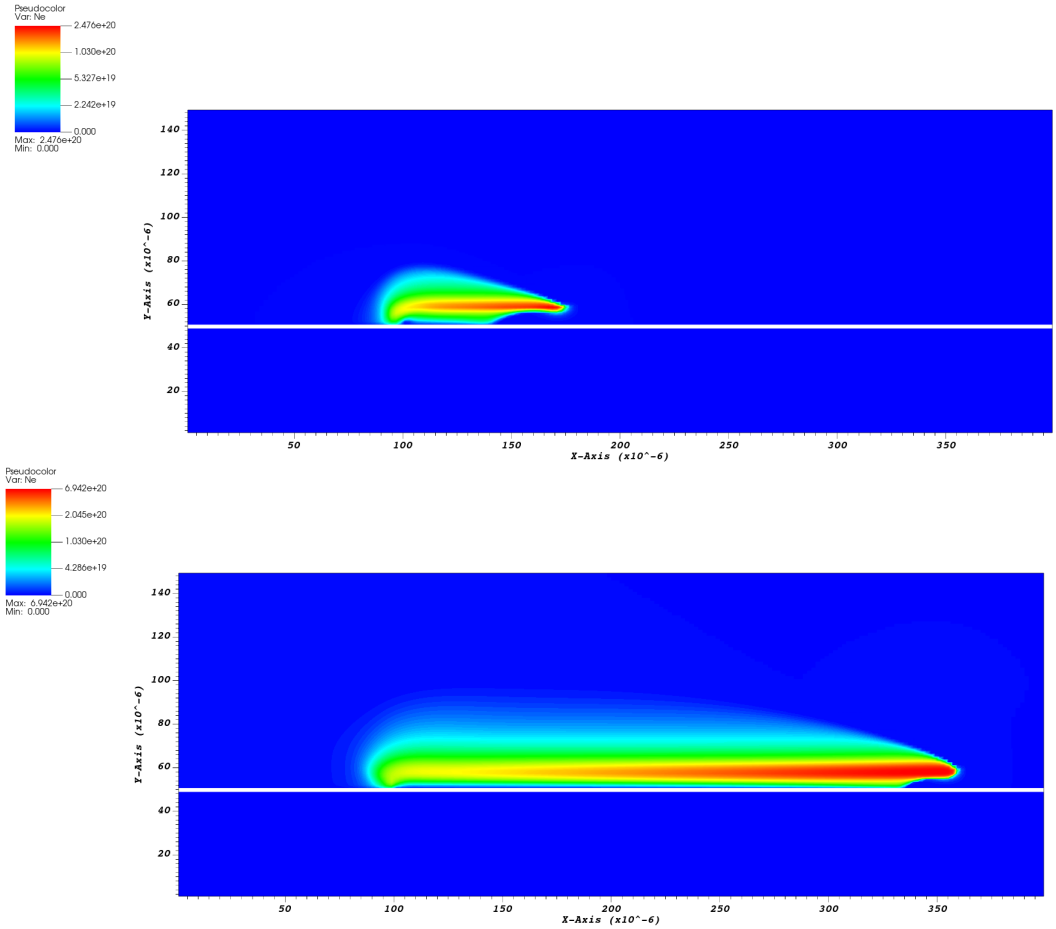

Figure 4.23: Electron density n_e $[m^{-3}]$ at 40 ns with $V = 1kV$ (above) and $V = 2kV$ (below)

The maximum values for densities and body force for the two cases at 20 ns are compared in the table below:

$V\ [V]$	$\mathbf{F}_{max}\ [N/m^3]$	$n_{e,max}\ [m^{-3}]$	$n_{i,max}\ [m^{-3}]$
1000	$3 \cdot 10^{-3}$	$9.54 \cdot 10^{14}$	$2.2 \cdot 10^{17}$
2000	$6.6 \cdot 10^{-2}$	$9.92 \cdot 10^{20}$	$1.767 \cdot 10^{21}$

Table 4.4: Evolution of maximum values with supply voltage

These results are in agreement with other studies [20, 23], a higher input voltage generates a faster ionic wind and a stronger body force imparted on the neutral, therefore improving its effect on the airflow. However too high voltages are no longer efficient from a costs perspective and they increase heating locally which could lead to damages to heat sensitive components. This is the reason why, typically in AC operations the voltage is kept constant while the frequency is increased, leading to the same result but without the negative aspects.

Chapter 5

Conclusions

In this thesis, we presented a numerical, physical, and chemical model describing a Dielectric Barrier Discharge plasma actuator. The main objective of this model is to qualitatively represent the most prominent features of the plasma discharge produced by the actuator, such as its development over time and the force induced on the external flow. In order to achieve such outcome, as well as to reduce computational times and costs, several approximations are introduced. Said approximations have been proven, in the different studies cited throughout this paper, to not have a great effect in the results, at least from a phenomenological point of view. The only exceptions are the Local Field Approximation, which could become inaccurate at high frequency levels, and the neglect of photoionization, which is a very important process in plasma dynamics. However, in order to not excessively complicate the model, they have been considered acceptable for the level of accuracy desired from this study. We then implemented this model into a numerical code capable of solving the governing equations of DBD physics. Despite dielectric relaxation time and chemical reaction rates being rather limiting when it comes to integration time steps, it was possible to obtain stable and accurate solutions with time steps 40-50 times larger.

The first test case presented consists in the most simple one possible: a direct current energy supply, an exposed anode, and standard input parameters. This allowed us to verify the accuracy of the model and observe the most essential features of plasma discharge.

In the second simulation, through the inversion of the anode with the cathode, we were able to study the role of the asymmetrical positioning of the two electrodes. It can be concluded that this geometrical asymmetry leads to an asymmetry in the plasma processes that take place during the discharge.

We then analyzed the behaviour of charge and number densities and body force in time by comparing two similar cases, Case 1 and Case 3. These parameters grow in the first stage of the discharge when avalanche ionization is still the dominant

chemical process; moving away from the exposed electrode, their growth rate slows down, the force eventually even decreases in intensity due to a weaker electric field and chemical reactions that reduce the number of free electrons and ions.
Two more simulations were conducted to study the influence of relative dielectric permittivity on DBD actuation. For higher levels of ϵ_r, the generated body force increases due to a stronger electric field. This result is in agreement with that of Forte et al. in [23]; the trend, however, is only true at lower voltages ($< 15kW$), because at greater voltages, a high permittivity value produces an electric field so strong that it becomes unstable and the discharge filamentary therefore reducing the efficiency of the actuator and generating unpredictable effects on the airflow.
Finally, the last case studies the influence of voltage amplitude on the discharge. We concluded that a higher voltage means a stronger body force. This increases the actuator's efficiency only within a certain voltage range, after which DBDs consume too much power and become too costly.

Further progress can be made using this code, both in accuracy and by analyzing more complex cases. Considering photoionization by introducing an artificial ionization term and implementing a non-uniform adaptive mesh could greatly increase results accuracy without complicating the process excessively. The study of DBD operation under an AC or gaussian pulse energy supply could be possible by properly modifying the code: it becomes necessary to consider a gradient in electron temperature and to implement a more complex chemical model that would introduce negative ions and other reactions, such as attachment processes.

Bibliography

[1] Z. Zhu. «Simulation of Flow Control using Dielectric-Barrier-Discharge (DBD) Plasma Actuators». PhD thesis. Irvine: University of California, 2023 (cit. on pp. 1, 4, 8, 10).

[2] G. Touchard. «Plasma actuators for aeronautics applications - State of art review». In: *International Journal of Plasma Environmental Science and Technology* 2.1 (2008), pp. 8–24 (cit. on pp. 1, 12).

[3] P. Gibbon. «Introduction to Plasma Physics». In: *Proceedings of the 2014 CAS-CERN Accelerator School* 1 (2016) (cit. on p. 2).

[4] T. Unfer, J.P. Boeuf, F. Roger, and F. Thivet. «An asynchronous scheme with local time stepping for multi-scale transport problems: Application to gas discharges». In: *Journal of Computational Physics* 227 (2007) (cit. on pp. 2, 30).

[5] T. Corke. «Single dielectric barrier discharge plasma enhanced aerodynamics: Physics, modeling and applications». In: *Experiments in Fluids* 46.1 (2009) (cit. on p. 2).

[6] U. Kogelschatz. «Atmospheric-pressure plasma technology». In: *Plasma Physics and Controlled Fusion* 46 (2004) (cit. on p. 2).

[7] X. Huang, S. Chan, X. Zhang, and S. Gabriel. «Variable structure model for flow-induced tonal noise control with plasma actuators». In: *AIAA Journal* 46.1 (2008), pp. 241–50 (cit. on p. 2).

[8] E. Peers, H. Xun, and L. Xinfu. «A Numerical Model of Plasma-Actuator Effects in Flow-Induced Noise Control». In: *IEEE Transactions of Plasma Science* 37.11 (2009), pp. 2250–56 (cit. on p. 2).

[9] H. Yu, A. Zhang, and J. Zheng. «Dynamic stall control for a vertical-axis wind turbine using plasma actuators». In: *AIAA Journal* 61.11 (2023), pp. 4839–51 (cit. on p. 2).

[10] N. Zouzou. «Dielectric barrier discharge type electrostatic precipitators - An overview». In: *International Journal of Plasma Environmental Science and Technology* 19 (2025) (cit. on p. 2).

[11] T. Kuwahara and Y. Asaka. «Fundamental characteristics of single dielectric barrier discharge plasma actuator using magnetic fluid». In: *International Jounral of Plasma Environmental Science and Technology* 17 (2023) (cit. on p. 2).

[12] R. Wang, E.J.M. van Heesch, Z. Liu, S. Li, and K. Yan. «Industrial dielectric barrier discharge plasma for odor control». In: *International Journal of Plasma Environmental Science and Technology* 19.2 (2025) (cit. on p. 2).

[13] M.D. Atkinson, J. Poggie, and J.A. Camberos. «Control of separated flow in a reflected shock interaction using a magnetically-accelerated surface discharge». In: *Physics of Fluids* 24.12 (2012) (cit. on p. 2).

[14] D.S. Tehrani, G.R. Abdizadeh, and S. Noori. «Numerical modeling of dielectric barrier discharge actuators based on the properties of low-frequency plasmons». In: *Scientific Reports* 12.1 (2022) (cit. on p. 2).

[15] C. He, T.C. Corke, and M.P. Patel. «Plasma flaps and slats: an application of weakly ionized plasma actuators». In: *Journal of Aircraft* 46.3 (2009), pp. 864–873 (cit. on p. 2).

[16] M. Visbal, D. Gaitonde, and S. Roy. «Control of Transitional and Turbulent Flows Using Plasma-based Actuators». In: *AIAA Journal* (2006), pp. 14–21 (cit. on p. 2).

[17] S. Ji, B. Zhang, J. Li, and G. Wang. «Numerical Study for Active Flow Control Using Dielectric Barrier Discharge Actuators». In: *Journal of Aerospace Engineering* 30.5 (2017), pp. 1–9 (cit. on pp. 2, 18).

[18] E. Moreau. «Airflow control by non-thermal plasma actuators». In: *Journal of Physics D: Applied Physics* 40 (2007) (cit. on p. 3).

[19] N. Bernard and E. Moreau. «Electrical and mechanical characteristics of surface AC dielectric barrier discharge plasma actuators applied to airflow control». In: *Experiments in Fluids* 55.1846 (2014) (cit. on p. 4).

[20] K.V. Karthikeyan and R. Harish. «Advancements in flow control using plasma actuators: a comprehensive review». In: *Engineering Research Express* 7 (2025) (cit. on pp. 4, 7, 9, 11, 12, 59).

[21] M.A. Barbosa Moreira, F.M. Freire Rodrigues, and J.C. Pàscoa Marques. «Experimental Study of Dielectric Barrier Discharge Plasma Actuators for Active Flow Control». In: *International Congress on Engineering - Engineering for Evolution* (2020), pp. 487–499 (cit. on p. 4).

[22] H. Aono, S. Sekimoto, M. Sato, A. Yakeno, T. Nonomura, and K. Fuji. «Computational and experimental analysis of flow structures induced by a plasma actuator with burst modulations in quiescent air». In: *Mechanical Engineering Journal* 2.4 (2015) (cit. on pp. 5, 8).

[23] M. Forte, J. Jolibois, J. Pons, E. Moreau, G. Touchard, and M. Cazalens. «Optimization of a dielectric barrier discharge actuator by stationary and non-stationary measurements of the induced flow velocity: application to airflow control». In: *Experiments in Fluids* 43.917 (2007) (cit. on pp. 5, 7, 59, 61).

[24] A. Salmasi, A. Shadaram, and A.S. Taleghani. «Effect of Plasma Actuator Placement on the Airfoil Efficiency at Poststall Angles of Attack». In: *IEEE Transactions of Plasma Science* 41.10 (2013), pp. 3079–85 (cit. on p. 6).

[25] A. Likhanskii, R.B. Miles, and M.N. Shneider. «Modeling of Interaction Between Weakly Ionized Near-Surface Plasmas and Gas Flow». In: *44th AIAA Aerospace Sciences Meeting and Exhibit* Reno, Nevada (2006) (cit. on pp. 8, 37).

[26] M. Hasan and M. Atkinson. «Investigation of a Dielectric Barrier Discharge Plasma Actuator to Control Turbulent Boundary Layer Separation». In: *Applied Sciences* 10.1911 (2019) (cit. on p. 8).

[27] S. Kabirian and A. Jahangirian. «Active Flow Control Using DBD Plasma Actuators in order to Reduce Trailing Edge Wakes in Wind Farms». In: (2020), pp. 3–4 (cit. on p. 8).

[28] D.M. Orlov. «Modelling and Simulation of Single Dielectric Barrier Discharge Plasma Actuators». PhD thesis. Indiana: University of Notre Dame, 2006 (cit. on p. 8).

[29] Y.B. Suzen, P.G. Huang, J.D. Jacob, and D.E. Ashpis. «Numerical simulations of plasma based flow control applications». In: *35th AIAA Fluid Dynamics Conference and Exhibit* Toronto, Ontario (2005) (cit. on p. 8).

[30] R.A. Bernal-Orozco, I. Carvajal-Mariscal, and O.M. Huerta-Chavez. «Flow and performance effects of a phenomenological model for a DBD actuator under different operating parameters». In: *Journal of the Brazilian Society of Mechanical Sciences and Engineering* (2023) (cit. on p. 9).

[31] T. Brauner, S. Laizet, N. Bernard, and E. Moreau. «Modelling of Dielectric Barrier Discharge Plasma Actuators for Direct Numerical Simulations». In: *8th AIAA Flow Control Conference* Washington DC (2016) (cit. on pp. 9, 36).

[32] B. Parent, M. Schneider, and S. Macheret. «Detailed Modeling of Plasmas for Computational Aerodynamics». In: *AIAA Journal* 54.1 (2016), pp. 1–14 (cit. on p. 10).

[33] B. Jayaraman and W. Shyy. «Modeling of dielectric barrier discharge-induced fluid dynamics and heat transfer». In: *Progress in Aerospace Sciences* 44 (2008), pp. 139–191 (cit. on p. 10).

[34] D. Giordano. «Hypersonic-Flow Governing Equations with Electromagnetic Fields». In: *33rd Plasmadynamics and Lasers Conference* (2002) (cit. on p. 10).

[35] J.S. Shang. «Recent research in magneto-aerodynamics». In: *Progress in Aerospace Sciences* 37 (2001), pp. 1–20 (cit. on p. 10).

[36] J.J. Wang, K.S. Choi, L.H. Feng, T.N. Jukes, and R.D. Whalley. «Recent developments in DBD plasma flow control». In: *Progress in Aerospace Sciences* 62 (2013) (cit. on pp. 11, 12).

[37] M. Abdullah, M.T. Galib, M.S. Ali Khan, T. Rahman, and M.M. Hossain. «Recent advancements in flow control using plasma actuators and plasma vortex generators». In: *Heat Transfer* 53.8 (2024) (cit. on p. 12).

[38] B. Karadag, C. Kolbakir, and A.S. Durna. «Plasma actuation on a NACA 4412 airfoil». In: *Aircraft Engineering and Aerospace Technology* 93.10 (2021) (cit. on p. 13).

[39] A. Abdelaziz, T. Ishijima, N. Osawa, and T. Seto. «Quantitative analysis of ozone and nitrogen oxides produced by a low power miniaturized surface dielectric barrier discharge: effect of oxygen content and humidity level». In: *Plasma Chemistry and Plasma Processing* 39.1 (2019) (cit. on p. 13).

[40] R. Arpa. «Physical and numerical modeling of Dielectric Barrier Discharge actuators for flow control problems». PhD thesis. Politecnico di Torino, 2011 (cit. on pp. 13, 19, 34, 36).

[41] I.A. Kossyi, A.Yu. Kostinsky, A.A. Matveyev, and V.P. Silakov. «Kinetic scheme of the non-equilibrium discharge in nitrogen-oxygen mixtures». In: *Plasma Sources Science and Technology* 1.3 (1992), pp. 207–220 (cit. on pp. 15, 25).

[42] G.I. Font and W.L. Morgan. «Recent Progress in Dielectric Barrier Discharges for Aerodynamic Flow Control». In: *Contributions to Plasma Physics* 47.1-2 (2007), pp. 103–110 (cit. on p. 15).

[43] K.S. Thorne and R.D. Blandford. *Applications to Classical Physics*. California Institute of Technology, 2012 (cit. on pp. 17, 19).

[44] D. Redchyts, O. Polevoy, S. Moiseienko, N. Starun, N., V. Zaika, and O. Akimenko. «New Mathematical Model of Dielectric Barrier Discharge Plasma Actuator in Air». In: Jan. 2023, pp. 168–176 (cit. on p. 18).

[45] Y. Lagmich M. Ouali. «Numerical Modeling of a Dielectric Discharge Plasma Actuator Using Local Energy Approximation for Application to Flow Control». In: *Mathematical Modelling of Engineering Problems* 11.7 (2024) (cit. on p. 18).

[46] A. Popoli, F. Ragazzi, G. Pierotti, G. Neretti, and A. Cristofolini. «A Boltzmann Electron Drift Diffusion Model for Atmospheric Pressure Non-Thermal Plasma Simulations». In: *Plasma* 6 (2023) (cit. on p. 18).

[47] T.C. Dias and V. Guerra. «Are local-field and local-energy approximations appropriate for modeling nanosecond discharges?» In: *Journal of Applied Physics* 58 (2025) (cit. on p. 20).

[48] *Bolsig+*. `https://www.bolsig.laplace.univ-tlse.fr/index.html` (cit. on p. 21).

[49] S.O. Macheret, M.N. Shneider, and R.B. Miles. «Modeling of air plasma generation by repetitive high-voltage nanosecond pulses». In: *IEEE Transactions on plasma science* 30.3 (2002) (cit. on p. 22).

[50] C. Punset, S. Cany, and J.P. Boeuf. «Addressing and sustaining in alternating current coplanar plasma display panels». In: *Journal of Applied Physics* 86.1 (1999) (cit. on pp. 31, 32).

[51] P. Ferrero and D. D'Ambrosio. «A numerical method for conjugate heat transfer problems in hypersonic flows». In: *40th AIAA Thermphysics Conference* Seattle, WA (June 2008) (cit. on p. 31).

[52] G. Strang. «On the Construction and Comparison of Difference Schemes». In: *SIAM Journal on Numerical Analysis* 5.3 (1968), pp. 506–517 (cit. on p. 32).

[53] R.J. LeVeque. *Finite Volume Methods for Hyperbolic Problems*. Cambridge, UK: Cambridge University Press, 2004 (cit. on pp. 32, 33).

[54] R. Arpa and D. D'Ambrosio. «High-Order Accurate Implicit Scheme for Drift-Diffusion Equations and Application to Dielectric Barrier Discharges». In: *American Institute of Aeronautics and Astronautics* (2017) (cit. on p. 33).

[55] W.R. Frensley. «Scharfetter-Gummel Discretization Scheme for Drift-Diffusion Equations». In: (2004) (cit. on p. 33).

[56] T.D. Nguyen, C. Besse, and F. Rogier. «High-order Scharfetter-Gummel-based schemes and applications to gas discharge modeling». In: *Journal of Computational Physics* 461 (2022) (cit. on p. 33).

[57] National Institute of Standards and Technology. *2nd order Runge-Kutta (RK2)*. `https://www.ctcms.nist.gov/~langer/oof2man/RegisteredClass-RK2.html` (cit. on p. 35).